

# Quasars as Absorption Probes of the J0053+1234 Region<sup>1</sup>

Daniel H. McIntosh<sup>2</sup>, Chris D. Impey, and Catherine E. Petry

*Steward Observatory, University of Arizona, 933 North Cherry Avenue, Tucson, AZ 85721*

*dmac@hamerkop.astro.umass.edu, cimpey@as.arizona.edu, cpetry@as.arizona.edu*

## ABSTRACT

We present *UBRI* photometry and spectra for 60 quasars found within one square degree centered on the J0053+1234 region, which has been the subject of the Caltech Faint Galaxy Redshift Survey. Candidate quasars were selected by their ultraviolet excess with respect to the stellar locus, and confirmed spectroscopically. The quasars span a wide range in brightness ( $17.5 < B < 21.6$ ) and redshift ( $0.43 < z < 2.38$ ). These new quasars comprise a grid of absorption probes that can be used to study large-scale structure as well as the correlation between luminous galaxies, non-luminous halos, and Lyman- $\alpha$  absorbers in the direction of the deep pencil-beam galaxy survey. Spectra of 14 emission line galaxies found using the same technique are also presented.

*Subject headings:* quasars: emission lines — surveys — catalogs

## 1. Introduction

Pencil-beam galaxy redshift surveys are enormously useful in defining the evolution and clustering of luminous matter out to redshifts  $z \gtrsim 1$ . An important complement to such surveys is a network of quasar absorbers within the same volume, which allows the detection of matter in absorption that would be impossible to detect in emission. Leveraging a large investment of resources from the Hubble Space Telescope (*HST*), the two Hubble Deep Fields (HDF-N and HDF-S Williams et al. 1996, 2000) have attracted an international campaign of multi-wavelength observations. The more recent Ultra-Deep Field (UDF) is attracting similar attention. The Caltech Faint Galaxy Redshift Survey (CFGRS) has devoted a concentrated effort to two fields, using the Low Resolution Imaging Spectrograph at the Keck Observatory (Cohen et al. 1996). One CFGRS field is the northern Hubble Deep Field, and the other is a previously unstudied field centered at  $\alpha = 00^{\text{h}}53^{\text{m}}23^{\text{s}}$ ,  $\delta = 12^{\circ}33'58''$

(J2000). Initial spectroscopy has been published by Cohen et al. (1999a,b), and a clustering analysis based on both fields has also been presented (Hogg, Cohen, & Blandford 2000). These studies concentrate on the distribution and evolution of luminous matter along this sightline, and will eventually reveal the evolutionary properties of galaxies of different Hubble types, delineate large-scale structure in redshift, and help define the cosmic history of star formation. Here we provide a grid of quasar probes, which will allow an examination of the cold, diffuse, and dark components of the universe along the J0053+1234 pencil beam.

Regardless of the depth of an imaging survey, it can reveal only the luminous parts of galaxies, which contain about 10–15% of the baryons in the local universe, which in turn form only about 15% of the matter content of the universe (Turner 2001). Studying the cold, diffuse, and dark components of the universe in a cosmological volume centered on J0053+1234 provides an important complement to the study of the luminous matter content. This can be accomplished by absorption line spectroscopy, using distant quasars as probes. For example, galaxy halos can be detected indirectly using the C IV  $\lambda\lambda 1548, 1550$  and Mg II  $\lambda\lambda 2796, 2800$  doublets over the entire range  $0 < z < 4$  (e.g. Meylan 1995). Furthermore, Lyman- $\alpha$  absorbers are as numerous as galaxies and they effectively trace the

<sup>1</sup>Observations reported here were obtained at Kitt Peak National Observatory, National Optical Astronomy Observatories, which is operated by the Association of Universities for Research in Astronomy, Inc., under cooperative agreement with the National Science Foundation.

<sup>2</sup>Present address: University of Massachusetts, Lederle Graduate Research Tower, Amherst, MA 01003

gravitational potential of the underlying dark matter (Miralda-Escudé et al. 1996; Croft et al. 1998). Given a sufficiently bright background quasar, absorbers can be detected with an efficiency that does not depend on redshift. In this respect, quasar absorption probes have an advantage over galaxy surveys that are always affected by, and sometimes compromised by, effects such as cosmological  $(1+z)^4$  dimming,  $k$ -corrections, and morphological selection that depends on redshift.

The detection of a network of quasar absorbers in a volume that encompasses a deep pencil-beam survey allows measurements of large-scale structure that can be used to relate luminous baryons in galaxies to baryons that are largely intergalactic. Individual quasar sightlines show that metals such as C IV and Mg II have correlation power on scales up to  $100 h_{100}^{-1}$  Mpc (Loh, Quashnock & Stein 2001), and multiple sightlines have been used to trace out three-dimensional structures on even larger scales (Dinshaw & Impey 1996; Williger et al. 1996). Locally, a grid of quasar probes have been used to trace out diffuse gas structure in three dimensions and relate it to the galaxy distribution in the direction of the galactic poles (Vanden Berk 1999) and in the direction of the Virgo cluster (Impey, Petry, & Flint 1999). There is evidence that Lyman- $\alpha$  absorbers are significantly but weakly clustered on scales of 20-30  $h_{100}^{-1}$  Mpc (Williger et al. 2000; Liske et al. 2000). Deep pencil-beam galaxy redshift surveys have shown that around half of the bright galaxies lie in high contrast structures with line of sight separations of 50-300  $h_{100}^{-1}$  Mpc (Cohen et al. 1996, 1999a). Thus, the spatial relationship between quasar absorbers and luminous galaxies can be studied as a function of redshift. Gas dynamical simulations indicate that low column density absorbers more closely reflect the underlying dark matter mass distribution than galaxies (Cen et al. 1998).

We have already published first results on a quasar survey in an area encompassing the HDF-N (Liu et al. 1999; Vanden Berk et al. 2000), and we are completing a multi-color search for quasars in a region centered on the HDF-S (see also Palunas et al. 2000). In this paper, we present the observations that have led to the discovery of 60 quasars in a one square degree field centered on the J0053+1234 region of Cohen et al. (1999a,b). The galaxy redshift survey covered a region  $14.6 \text{ arcmin}^2$  at the center of the field surveyed for quasars. In all three cases, quasar selection is a prelude to absorption line spectroscopy and a comparison of the spatial distribution of absorbers and galaxies.

Although quasars as faint as  $B \approx 21.5$  have traditionally been too challenging for absorption line work, a new generation of large ground-based telescopes and multi-object spectrographs will enable the follow-up observations required for this sample.

We describe the imaging and multi-color photometry leading to the selection of quasar candidates in §2, and the quasar candidate selection in §3. In §4 we describe the spectroscopy. In §5 we summarize the yield of confirmed quasars, the reliability of the redshifts, and present a smaller number of emission line galaxies discovered in the same survey. We close with brief comments on future work on this region. A second paper (Petry, Impey, & McIntosh, in preparation) will present additional quasar candidates for the J0053+1234 field derived from deeper  $U$  imaging of the central half square degree, as well as confirmed quasars in the entire field from two recent observing runs. Additional papers will present photometry, quasar candidate lists, and confirmed quasars for both the Hubble Deep Fields, North and South. Spectra have been obtained for quasars in all three fields that are of sufficient quality to measure strong Lyman- $\alpha$  absorbers, so these future papers will also include a first comparison between quasar absorbers and galaxies in the three pencil-beam surveys.

## 2. Photometry

### 2.1. Observations

We used the Kitt Peak National Observatory (KPNO) 0.9-meter Telescope with the CCD Mosaic Wide-Field Imager (Boroson et al. 1994; Muller et al. 1998) to acquire  $UBRI$  observations of the one square-degree region centered on the J0053+1234 region ( $\alpha = 00^{\text{h}}53^{\text{m}}23.2^{\text{s}}, \delta = +12^{\circ}33'58''$ ) during 1998 September 30 – October 2 UT, under generally good observing conditions.

The Mosaic imager has eight  $2048 \times 4096$  pixel anti-reflection coated SITe Loral chips. The combined field of view spans  $59' \times 59'$ , and has a pixel scale of  $0''.43$  ( $15 \mu\text{m}$  pixels). The readout noise for this camera is  $5.66e^-$ , the dark current is negligible ( $\sim 15e^- \text{ hour}^{-1}$ ), and the average single chip gain is  $2.86e^- \text{ ADU}^{-1}$ . Each CCD has been thinned for detecting  $U$ -band photons; however, the quantum efficiency (QE) still falls off rapidly blueward of  $4000 \text{ \AA}$ . Thus, the spectral response in the  $U$ -band is not a perfect match to standard Johnson (1966)  $U$ -band. The Mosaic camera employs a large (5.75 inches square)

par-focal filter set. Each filter’s transmission and response, calculated from the QE, is plotted in Figure 1.

An area of sky centered on the J0053+1234 region was imaged in each passband using a standard dither pattern with five separate pointings a few arcminutes apart to remove inter-chip gaps, CCD defects and cosmic rays. This dither pattern ensured at least 80% of the maximum exposure for all regions of a final combined image of 5 exposures. The total integration times were 420, 110, 30, and 70 minutes for the  $U$ ,  $B$ ,  $R$  and  $I$  bands, respectively. A variety of short and long exposure times were used for individual  $U$  and  $I$  frames to avoid saturation of the brightest objects. Unfortunately, we did not experience perfectly photometric conditions during our imaging campaign. Nevertheless, for relative photometric calibration we imaged Landolt (1992) standard star cluster fields, over a range of airmasses, at least three times during each night. The overall photometric zero point consistency was  $\sim 10\%$ . Quasar selection is governed by relative colors with respect to the stellar locus; therefore, zero point determination did not limit our ability to identify quasar candidates with this photometry. We summarize the observations in Table 1.

## 2.2. Data Reduction

To select quasar candidates in the J0053+1234 region for spectroscopic follow-up, we require good photometric uniformity across our deep, wide-field images. Homogeneous photometry also requires procedures to deal with bad pixels, cosmic rays, and gaps between CCD’s in each passband. Achieving such high quality images requires stacking dithered Mosaic frames, which in turn places high demands on the initial data reduction steps<sup>3</sup>. In particular, the data must be well-flattened and carefully corrected for photometric effects of the variable pixel scale. The data are reduced with a customized reduction pipeline that uses the IRAF<sup>4</sup> environment and adheres to standard image reduction techniques.

We perform basic reduction of the individual Mosaic frames using the IRAF *mscred* package. This software allows image processing to be performed on multi-chip exposures as if they were single CCD

frames. For each single Mosaic exposure, we trim and debias the eight individual chip images separately. A small correction ( $< 0.3\%$ ) is necessary due to cross talk between pairs of adjacent chips sharing the same electronics in the Mosaic detector. This correction subtracts a predetermined fraction of the adjacent chip’s  $(i, j)^{\text{th}}$  pixel value from pixel  $(i, j)$  of the current chip. We then remove an averaged zero frame from each Mosaic image. The thinned Mosaic chips require no dark correction. Roughly 0.4% of the full array of  $8192 \times 8192$  pixels are bad; these are flagged and included in the mask frames during the final image combination.

An important step towards achieving precise photometry is the determination and removal of the response function of the individual CCD’s – *i.e.* flat fielding the data. Traditionally, dividing each exposure by a uniformly illuminated blank frame will produce an image that has a uniform and flat appearance. Yet, the Mosaic imagers have pixel scales that decrease roughly quadratically such that an individual pixel in a field corner is 6% smaller, and contains only 92% of the flux, compared to a pixel at field center (see MosManual for details). Therefore, although an individual star anywhere on the image will have the same number of photons within the point-spread-function (PSF), the variable pixel scale causes the photometric zero point to vary by 8% over the field of view. We correct for this photometric effect following the recommendations given in the MosManual. Briefly, we flatten each image with a flat-field frame that has *not* been corrected for the variable pixel scale. Then, following our astrometric calibration and prior to stacking multiple exposures, we re-grid each frame to a tangent-plane projection with pixels of constant angular scale. We note that during the re-gridding, we *do not* scale each pixel photometrically by the amount each pixel area has changed. In this manner we account for the variable pixel scale and produce uniform images over the entire field of view.

We construct flat-field frames for each passband using a combination of twilight and night-sky flats. First we make a normalized flat with high signal-to-noise (S/N) by averaging a set of twilight illuminated exposures. This component accounts for both the small scale, high frequency (pixel-to-pixel) variations in response, and the spatial variations over large fractions of an image. We then fit a smooth surface to a night-sky flat produced by median combination of a set of unflattened frames of the J0053+1234 region with all

<sup>3</sup>NOAO CCD Mosaic Imager User Manual (hereafter MosManual), Version Sept. 15, 2000, G. Jacoby; <http://www.noao.edu/kpno/mosaic/manual/index.html>.

<sup>4</sup>IRAF is distributed by the National Optical Astronomical Observatories, which are operated by AURA, Inc. under contract to the NSF.

objects masked out, and we multiply this smooth surface to the twilight flat frame to produce a high S/N flat with the spectral response of the night sky. We iterate the flat field construction twice to optimize the night-sky flat object masking. Thus, the resultant “super flat” for each passband is spatially and spectrally flat. We divide each exposure of the J0053+1234 region and the standard star cluster image by its super flat to achieve  $\lesssim 1\%$  global flatness over the eight chip array.

Good astrometry is required to register and stack each dithered set of exposures. In addition, accurate celestial coordinates are necessary for the follow-up spectroscopy of identified quasar candidates. All Mosaic images have an initial default world coordinate system (WCS) loaded in their header at the time of observation. The WCS maps the image pixel space onto celestial coordinate axes (RA and Dec). However, effects such as global pointing offsets, instrument rotations and differential atmospheric refraction produce the need for corrections to this astrometric calibration. We use the *mscmatch* package in IRAF to interactively derive accurate ( $\text{RMS} \lesssim 0.3''$ ) astrometric solutions for each dithered exposure by matching  $\sim 300$  fairly bright stars (blue and red magnitudes  $12 \lesssim m \lesssim 16.5$ ), distributed evenly over the Mosaic field, with a reference frame given by their epoch J2000.0 USNOv2.0 coordinates (Monet et al. 1996). We map the eight chip exposures for each Mosaic frame onto a single image by rebinning the pixels to a tangent-plane projection, thus producing pixels of constant angular size (as described above). The resultant image is astrometrically calibrated to the J2000.0 celestial equatorial WCS.

Finally, we combine each set of fully processed and registered exposures into a final high S/N image for each passband. We subtract a constant flux level equal to the mode sky value from each image in a dithered set. Higher order terms are unnecessary due to the better than 1% global flat fielding. Before combining a dithered sequence of exposures into a single image, we account for the different photometric depths of individual frames. These differences are due to time-varying effects during observations. The most common effect is the changing airmass over an hour-long dithered sequence. Variable sky transparency due to occasional thin clouds (cirrus) is a second effect. All exposures of a dithered sequence are scaled to the reference image selected to have the lowest airmass and/or best photometric conditions. We calculate each frame’s mul-

tiplicative scale factor by comparing simple aperture flux measurements from the set of  $\sim 300$  astrometric calibration stars common to each image and its reference. The scaling factors are typically of order a few percent. This procedure scales each set of dithered, same passband frames to the same effective airmass and exposure time (given in Table 2). We align and median combine (for removal of cosmic rays) each dithered set of registered, scaled, and sky-subtracted J0053+1234 region Mosaic frames to produce calibrated and cosmetically clean images.

### 2.3. Calibrations and Catalogs

We use the source detection and extraction software SExtractor (Source Extractor; Bertin & Arnouts 1996) to compile catalogs of instrumental magnitudes (MAG\_BEST) for every source in the final *UBRI* images. In addition, SExtractor provides accurate positions and a variety of photometric measurements for each detected source. We configure SExtractor to detect objects comprised of a minimum of 5 pixels (DEBLEND\_MINAREA) above a background threshold of  $3\sigma_{\text{bkg}}$  (DETECT\_THRESH). Overlapping sources are deblended into multiple objects if the contrast between flux peaks associated with each object is  $\geq 0.05$  (DEBLEND\_MINCONT). These parameters provide our working definition of an imaged source. We confirm that these parameters provide good source detection and deblending by visually inspecting random regions from each image. We remove sources from each catalog with saturated, or otherwise corrupted, pixel values as flagged by SExtractor ( $\text{FLAGS} \geq 4$ ). The primary source of flagged sources are those with bright magnitudes; i.e. have at least one saturated pixel. Additionally, we exclude sources within 140 pixels ( $60''$ ) of an image edge; stacking and combining dithered frames makes these regions of the final images lower in S/N.

We determine a turn-over magnitude ( $m_{\text{TO}}$ ) where the source counts distribution flattens and begins to fall off. This empirical limit provides a rough estimate of the magnitude that all sources, point-like and extended, become incomplete. For point sources we estimate 99% and 90% completeness limits by randomly distributing artificial stars in each image (100 per  $\Delta m = 0.25$  bin over the magnitude range  $m_{\text{TO}} - 1 \leq m \leq m_{\text{TO}} + 2$ ), rerunning SExtractor, and determining the number of these stars that are recovered. We use the IRAF *artdata* package to create artificial stars with characteristics (PSF size, magnitude zero

point, gain, and Poisson noise) matched to actual stars on our images. We note that extended source completeness is more difficult to quantify, due mostly to the wide range of galaxy surface brightnesses. For this reason, the completeness of extended sources turns over more slowly than for point sources. As can be seen in Table 3, the 90% completeness limit for point sources is fainter than  $m_{\text{TO}}$ .

We summarize the magnitude limits and number counts for the sources in the separate  $U$ ,  $B$ ,  $R$ , and  $I$  catalogs in Table 3. To generate the catalogs from which quasar candidates will be selected, we sequentially match the  $U$  catalog with the  $B$ ,  $R$ , and finally the  $I$  source catalogs. We note that in all four cases we use the entire (i.e. not magnitude-limited) catalogs. The 1946  $U$  sources are correlated with the  $B$  sources resulting in 1730  $UB$  matches with 216  $U$ -only sources (see discussion in §3). Comparing the  $UB$  matches with the  $R$  catalog results in 1642  $UBR$  matches, leaving 88  $UB$  matches without  $R$  magnitudes. Comparing the  $UBR$  matches with the  $I$  catalog results in 1552  $UBRI$  matches, leaving 90  $UBR$  matches without  $I$  magnitudes. Our final two source catalogs include all sources with reliable photometry. They are (1) the  $UBRI$  catalog with the 1552 matches in the  $UBRI$  bands, and (2) the  $UB$  catalog consisting of the 178 sources with no  $I$  magnitudes, of which 88 have neither  $R$  nor  $I$  magnitudes.

We transform science image fluxes into apparent magnitudes calibrated to the Landolt (1992) system. Even though the observing conditions were not photometric, calibrating the photometry to within  $\sim 25\%$  absolute provides useful flux estimates for the followup spectroscopic observations. The photometric system is defined by the zero point  $zp$ , extinction (or airmass) coefficient  $\alpha$ , and color coefficient  $\beta$  for each passband. These coefficients are determined by solving simple, linear transformation equations that relate instrumental magnitudes ( $u, b, r, i$ ) of standard stars observed each night with their published magnitudes ( $U, B, R, I$ ). We measure the fluxes of standard stars within a  $14''.4$  circular aperture similar to that used by Landolt (1992). We use IRAF's *photcal* package to find the best-fit solutions to the following transformation equations:

$$U = u + zp_U + \alpha_U X_U + \beta_U (U - B) \quad (1)$$

$$B = b + zp_B + \alpha_B X_B + \beta_B (U - B) \quad (2)$$

$$R = r + zp_R + \alpha_R X_R + \beta_R (R - I) \quad (3)$$

$$I = i + zp_I + \alpha_I X_I + \beta_I (R - I) \quad (4)$$

We give the calibration coefficients and their errors in Table 2. The photometric zero point quantifies the gain and the total sensitivity of the telescope plus detector. The airmass term is a measure of the atmospheric extinction as a function of telescope altitude. The color term shows how well the instrumental system matches the Landolt (1992) system. We note that large uncertainties in coefficients (i.e. systematic zero point and airmass term errors in excess of 0.1 mag) indicate non-photometric conditions during the nights we observed standards.

From the instrumental magnitude  $m_A$  of each source in passband  $A$ , we first convert to apparent magnitude  $A = m_A + zp_A + \alpha_A X_A$ , using the coefficients given in Table 2. Next, we calculate the colors of each source by iteratively solving the following equations:

$$(U - B)_i = (U - B)_0 + (\beta_U - \beta_B) \cdot (U - B)_{i-1}, \quad (5)$$

$$(R - I)_i = (R - I)_0 + (\beta_R - \beta_I) \cdot (R - I)_{i-1}. \quad (6)$$

The initial colors  $(U - B)_0$  and  $(R - I)_0$  are derived simply from the apparent magnitudes. We iterate these calculations using color coefficients from Table 2 until the difference between successive iterations is  $\delta m \leq 0.001$  mag.

Finally, we correct our magnitudes and colors for Galactic extinction by applying reddening corrections using the dust maps of Schlegel, Finkbeiner & Davis (1998)<sup>5</sup>. These new maps are based on full-sky  $100\mu\text{m}$  emission from *COBE/DIRBE* and *IRAS/ISSA* observations and, thus, directly measure the Galactic dust content. The Schlegel, Finkbeiner & Davis (1998) data have orders of magnitude higher resolution (at  $6.1''$ ), and are  $\sim 2$  times more accurate than the traditional Burstein & Heiles (1982) reddening estimates based on neutral hydrogen 21 cm emission. The J0053+1234 field does not have large extinction; the local reddening  $E(B - V)$  ranges from 0.058 to 0.075, corresponding to mean extinction corrections of 0.37, 0.29, 0.18, and 0.13 mag for  $UBRI$  passbands, respectively. These corrections have a formal uncertainty of 10%.

The systematic errors of our photometry dominate over random errors, even at the faintest magnitudes. The systematic uncertainties in our photometry are due

<sup>5</sup>The authors have kindly made available the dust maps with user friendly software that outputs  $E(B - V)$  for an input  $(l, b)$  at <http://astron.berkeley.edu/davis/dust/index.html>.

mainly to the zero point calibration ( $\lesssim 0.10$  mag) and the airmass correction ( $\lesssim 0.10$  mag) resulting from the variable transparency during our observations. Yet, the obvious stellar locus of main sequence stars in the color-color plots (see §3) illustrate the utility of relative photometry during non-photometric conditions.

### 3. Quasar Candidate Selection

The practice of using multi-color photometry to search for quasars is well known (e.g. Koo, Kron, & Cudworth 1986; Hall et al. 1996; Liu et al. 1999). In this paper we present the full *UBRI* photometry, but only use the *U*, *B*, and *R* filters for quasar selection by ultra-violet excess, which is most efficient at  $z \lesssim 2.5$ . In future work the *I* information can and will be used to help select quasars at higher redshift, where the baseline to longer wavelengths is essential but the efficiency of selection is lower.

We plot our photometry for the 1552 sources from the *UBRI* catalog in two color-color plots: the  $(U - B)$  vs.  $(B - R)$  plane in Figure 2; and  $(U - B)$  vs.  $(R - I)$  in Figure 3. These sources have an effective cut of  $B = 21.3$  mag, corresponding to the limit of photometry accurate enough to define a tight stellar locus. In Figure 4 we plot the  $(U - B)$  vs.  $B$  color-magnitude diagram for the 1552 sources from the *UBRI* catalog plus the 178 additional sources from the *UB* catalog (i.e. only *U* and *B* detections). We note that the majority of sources from the *UB* catalog (plotted in Figure 4 as open circles) are bright ( $B < 17$  mag) and red ( $U - B > 0$ ). These bright *UB* sources are saturated in *R* and *I*, and they are both too bright and too red to be quasars. Also, 90 of these *UB* sources have *R* magnitudes but no *I* magnitudes, and so were not used in the  $(U - B)$  vs.  $(B - R)$  candidate selection process; however, this means that any quasars in this group of 90 will be found at a lower yield. We find 34 *UB* catalog sources scattered between  $16.0 < B < 19.5$  that are not part of the *UBRI* catalog for a variety of reasons: (i) 7 are edge sources in the *R* or *I* images<sup>6</sup>; (ii) 10 are flagged and removed from *R* or *I* owing to flux contamination from nearby bright red stars that are not contaminated at bluer passbands; and (iii) 17 are *I*-band saturated and thus, among the 90 *UBRI* detections. We note that it is possible that some of the 88 *UB* sources that were not detected in *R* may have been

detected in *I*; however, given the completeness limits of the survey, such objects must have an inflected spectrum and are therefore unlikely to be quasars with a power-law spectral energy distribution. Lastly, at faint  $B > 20$  limits there are blue  $(U - B) < 0.2$  *UB* catalog sources that are true *R* and *I*-band drop outs, many (30) of which meet our quasar candidate selection (see below) and were later targeted for spectroscopy (triangles in Figure 4; 16 are confirmed quasars shown as solid triangles).

Our primary selection strategy is based on  $(U - B)$  color, and thus depends on point sources detected jointly in at least *U* and *B*. However, there is an additional category of sources that are potentially of interest in a quasar selection experiment: *U*-only detections where the level of the *B* non-detection implies a source blue enough to be a quasar. Most of the 216 *U*-only sources are saturated stars or artifacts, and 53 of the 54 that are plausible point sources are faint,  $U > 21$ . Thus, the *U*-only faint sources are fainter than the sky brightness at longer wavelengths so they were considered too faint for useful spectroscopy. The omission of this category, which may include unrecognized quasars, affects the overall completeness measures that will be considered in an upcoming paper.

As illustrated in Figures 2 and 3, the stellar main-sequence is readily observed in color-color plots. The tight locus begins with cool stars at  $(U - B) \sim 1.4$  and ends abruptly at a blue color of  $(U - B) \sim -0.2$ , corresponding to the hottest main-sequence stars and white dwarfs. Quasars with  $z \lesssim 2$  have colors typically bluer than the stellar locus; therefore, following Liu et al. (1999) we select quasar candidates based on  $(U - B)$  color,  $(B - R)$  color, and *B* magnitude. The exact selection procedure is designed to maximize the efficiency of quasar selection relative to the stellar locus. We select *UBRI* quasar candidates in the *UBRI* catalog from two regions in the  $(U - B)$  vs.  $(B - R)$  plane as shown in Figure 2 by the dashed lines: Region 1 defined by  $(U - B) \leq -0.2$  and  $(B - R) \leq 0.6$ ; and Region 2 defined by  $(U - B) > -0.2$  and  $(B - R) \leq 0.4$ . In addition, we select the *UB* quasar candidates from the *UB* catalog with  $(U - B) \leq -0.1$ , as shown in Figure 4 by the dashed line.

We do not attempt to remove extended sources from our photometric catalogs. Many of the sources redward of the stellar locus in either color in Figures 2 and 3 are resolved; nevertheless, their removal to produce a tighter stellar locus is outweighed by the desire to keep all possible quasar candidates. When observed

<sup>6</sup>Our *UBRI* images are concentric to within a few tens of pixels ( $< 10''$ ), thus, a slight shift means some objects will be culled from one catalog given our edge proximity flag, yet not culled from another.

with sufficient resolution and S/N, many low redshift quasars appear non-stellar because of the presence of a host galaxy. In principle, any deep efficient search for quasars should apply a criterion that filters out the substantial number of faint galaxies while not rejecting quasars whose images are softened by host light. Yet, most of our quasar candidates are within two magnitudes of the detection limit. At these apparent brightnesses, the large CCD pixel scale and a slightly variable PSF (as a function of image position) cause SExtractor to be unreliable at distinguishing stars and galaxies. Specifically, we find that both our candidates and our confirmed quasars span the full range of the SExtractor star/galaxy classifier (CLASS\_STAR). For these reasons, we choose not to select according to CLASS\_STAR, and as a result, our sample has no explicit selection effect against quasars at low redshift or against quasars with luminous host galaxies.

We performed several empirical checks of the quality of our photometry across the large CCD field of view. The surface density of quasar candidates does not vary significantly across the field. Nor does the distribution of photometric errors, as might occur if there were position-dependent sensitivity or background variations. The variation of random photometric error with  $B$  magnitude is shown in the lower panel of Figure 4. All of this affirms the homogeneity of the photometry and the resultant catalogs.

## 4. Spectroscopy

### 4.1. Observations

We searched for quasars from the candidate list formed as described in §2.4 during two observing runs in the Fall of 2000. For the first run we used the Hydra multi-object spectrograph on the KPNO 3.5-meter WIYN telescope for 5 nights, 29 Sep – 3 Oct 2000. In two overlapping fields centered on the J0053+1234 region, we integrated for 13.5 and 18 hours each, observing 62 and 58 targets, respectively. We combined the Simmons camera using the blue fibers with the G400 grating to give wavelength coverage of about 3410–6610 Å, with a dispersion of  $1.56 \text{ Å pix}^{-1}$  and 6.8 Å resolution. We assigned approximately one third of the 100 Hydra fibers to observe the sky for optimum sky subtraction. During the second run at the MMT 6.5-meter on 30 Nov 2000 UT, we observed six targets from the candidate list for 20 min to 1 hour each, depending on the target brightness. For these observations, the Blue Channel spectrograph and the 300

1 mm<sup>-1</sup> grating (blazed at 5800 Å) provided wavelength coverage of about 3200–8800 Å, with a dispersion of  $1.94 \text{ Å pix}^{-1}$  and 8.8 Å resolution.

### 4.2. Data Reduction

The WIYN and MMT data are reduced with standard IRAF routines. We perform basic reduction of the CCD data using the *imred.ccdred* package. We trim, subtract the overscan region (fit with a low order Legendre polynomial), and bias subtract each CCD image. The dark current is low enough so that a correction is unnecessary. We flat field the MMT data by fitting a response function in the dispersion direction to a median-combined dome flat image and dividing it into the science images. Since only one exposure was taken of each MMT target, we create a bad pixel mask from the normalized flat field and use it to replace bad pixels in the science frames with flux values interpolated from nearby pixels.

For the WIYN data we perform the spectral extraction and calibration using the IRAF *dohydra* package in *imred.hydra*. We obtained dome flats for each of the two target configurations, which we use to trace the positions of the spectra on the chip for extraction as well as to determine the throughput correction. The apertures are referenced to the fibers so that the extracted spectra are properly identified. The flat field correction was performed by fitting an average spectrum over all the fibers in a configuration with a high order function. For wavelength calibration we calculate a wavelength solution from the HeNeAr lamp exposures taken adjacent in time to each science exposure. The solution is applied to the quasar candidate, sky, and standard star spectra. For each configuration, we visually inspect the set of sky spectra to be sure each sky position was free from contamination from non-sky sources. Then we construct an average of good sky spectra and subtract it from the science and standard star spectra. We observed the standard star BD+28°4211 for flux calibration of the science spectra. This star was observed only once during the run and the conditions were not photometric, therefore, the spectrophotometric calibration is only accurate to about 30% on average. More accurate spectrophotometry is not required for quasar identification since the distinguishing features are broad emission lines of large equivalent width.

We perform spectral extraction and calibration for the MMT data using *twodspec.longslit*. We extract the

science and standard star spectra by tracing the flux along the dispersion axis and subtracting a value for the sky. The sky is determined from a linear fit to sky pixels in a region transverse to the dispersion direction along the trace. We observed GD 50 as the flux standard to calibrate the science spectra. This star was only observed once during the run in non-photometric conditions. Thus, the flux calibration serves primarily to calibrate the continuum shape for the science targets, and the flux calibration does not yield spectrophotometry.

## 5. Results

### 5.1. Quasars

The number of quasar candidates selected from both the *UBRI* (Regions 1 and 2) and *UB* catalogs by the procedure described in §3 are listed in Table 4, along with the number of objects that were observed spectroscopically, and the number of confirmed quasars. From the *UBRI* selection, Region 1 was the most effective at finding quasars with an efficiency of 75% and a yield of 43 quasars; Region 2 only contributed one additional quasar among 11 targets observed. From the *UB* selection, 16 quasars were confirmed from 30 targets observed, for an efficiency of 53%. Overall, a total of 60 quasars were confirmed with an efficiency of 61%. To examine whether a color cut that included the blue end of the stellar locus would yield more quasars, we observed 12 of 15 sources spectroscopically with  $(U - B) \leq -0.1$  and  $0.4 < (B - R) \leq 0.6$ , but this selection yielded no additional quasars.

We measured the quasar redshifts and their rms errors by cross-correlating their spectra with the LBQS composite spectrum (Francis et al. 1991) using IRAF's *fxcor*. Figure 5 contains spectra of all objects where at least one broad emission line is detected, where we are essentially certain of the quasar identification. However, redshifts are not always as certain, particularly when only one emission line is observed. For spectral coverage in the range 3400–6400 Å, most redshifts yield two or more strong lines. The only exception in the range  $0.3 < z < 0.8$ , where Mg II is the strongest line, C III] and H $\beta$  are not covered, and [OII] might not be visible if it is weak. There are two cases (Q 005141+123050 and Q 005344+121847) where this occurs, and in each case the single strong line has only one plausible identification. Several other quasars in Figure 5 have their second strong line at the noisy,

blue end of the spectrum, but inspection of the data before clipping for display shows that the lines are real in each case. We note that three of the 60 spectra in Figure 5 were taken with the MMT which provides spectral coverage out to 8800 Å. In Figure 5 we clip these three spectra to 6750 Å and note that the only strong line omitted is Mg II in Q005501+125932, which has a secure redshift of  $z = 1.516$ .

The names of the new quasars, their J2000 coordinates, redshifts, and colors are listed in Table 5. Their spectra are plotted in R.A. order in Figure 5. The spectra have been smoothed with a Gaussian having a FWHM of 3 pixels, and the pixels at the bluest and reddest ends of the spectra which contain no useful information have been trimmed. Figure 6 shows a sky plot of the 60 quasars with the boundaries of the galaxy redshift survey of Cohen et al. (1999b) superimposed. To see if any quasar had been discovered previously, we performed a search in NED on the position of each quasar using a circular radius of 10 arcsec. Our survey did not rediscover any previously known quasar. NED lists an X-ray counterpart for Q005321+122740 and a radio counterpart for Q005355+121232, but redshifts for neither.

### 5.2. Emission Line Galaxies

Fourteen new narrow emission line galaxies were discovered in this survey. None were found in a search of NED. Their redshifts were measured by fitting a Gaussian profile to the three or four strong lines in each spectrum, computing the redshift for each line using the fitted line center, and averaging the redshifts determined for each spectrum. The ELG names, J2000 coordinates, redshifts, and colors are listed in Table 6. The second lowest redshift galaxy in the Table, Q005436+122318 has no colors listed because the nucleus and a nearby H II region were separately selected in the *B* band and *U* band images, respectively. The spectra are plotted in Figure 7, in R.A. order from left to right and down the page. The spectra have been smoothed with a Gaussian having a FWHM of 3 pixels, and the pixels at the bluest and reddest ends of the spectra which contain no useful information have been trimmed.

## 6. Future Work

We have presented the multi-color photometric selection and low-resolution spectroscopic confirmation of 60 new quasars in the J0053+1234 region. These



sources provide the initial grid of absorption probes for a cosmological volume centered on this region, which has been the subject of a deep redshift survey. These probes will be used in future work involving deep absorption spectroscopy to measure the relationship between massive halos traced by Mg II and C IV absorption, and those traced by luminous galaxies. Moreover, absorption in the spectra of these quasars will allow us to measure the bias between the baryons in the massive halos of luminous galaxies, and the baryons in the intergalactic medium traced by the Lyman- $\alpha$  forest of HI absorption. We have begun the deep absorption spectra observing campaign. Furthermore, we have selected additional quasar candidates based on deeper  $U$ -band imaging of the central half square degree of this region. The goal of the deeper imaging is to have a denser grid of absorption probes at small impact parameters from the field center, but spectroscopy of these additional quasars will be very challenging. Upcoming papers will address the overall completeness of our survey towards J0053+1234, and present additional quasar candidates and spectra.

## REFERENCES

- Bertin, E., and Arnouts, S. 1996, *A&AS*, 117, 39
- Boroson, T., Reed, R., Wong, W.-Y., and Lesser, M. P. 1994, *SPIE*, 2198, 877
- Burstein, D., and Heiles, C. 1982, *AJ*, 87, 1165
- Cen, R., Phelps, S., Miralda-Escudé, J., & Ostriker, J. P. 1998, *ApJ*, 496, 577
- Cohen, J. G., Cowie, L. L., Hogg, D. W., Songaila, A., Blandford, R. D., Hu, E. M., & Shopbell, P. 1996, *ApJ*, 471, L5
- Cohen, J. G., Hogg, D. W., Pahre, M. A., Blandford, R. A., Shopbell, P. L., & Richberg, K. 1999a, *ApJS*, 120, 171
- Cohen, J. G., Blandford, R. D., Hogg, D. W., Pahre, M. A., & Shopbell, P. 1999b, *ApJ*, 512, 30
- Croft, R. A. C., Weinberg, D. H., Katz, N., & Hernquist, L. 1998, *ApJ*, 494, 44
- Dinshaw, N., & Impey, C. D. 1996, *ApJ*, 458, 73
- Francis, P., et al. 1991, *ApJ*, 373, 465
- Hall, P. B., Osmer, P. S., Green, R. F., Porter, A. C., & Warren, S. J. 1996, *ApJ*, 462, 614
- Hogg, D. W., Cohen, J. G., & Blandford, R. 2000, *ApJ*, 545, 32
- Impey, C. D., Petry, C. E., & Flint, K. P. 1999, *ApJ*, 524, 536
- Johnson, H. L. 1966, *ARA&A*, 4, 193
- Koo, D. C., Kron, R. G., & Cudworth, K. M. 1986, *PASP*, 98, 285
- Landolt, A. U. 1992, *AJ*, 104, 340
- Liu, C. T., Petry, C. E., Impey, C. D., & Foltz, C. B. 1999, *ApJ*, 118, 1912
- Loh, J.-M., Quashnock, J. M., & Stein, M. L. 2001, *ApJ*, 560, 606
- Liske, J., Webb, J. K., Williger, G. M., Fernandez-Soto, A., & Carswell, R. F. 2000, *MNRAS*, 311, 657
- Meylan, G. 1995, editor, *ESO Workshop on QSO Absorption Lines*, Springer-Verlag: Berlin
- Miralda-Escudé, J., Cen, R., Ostriker, J. P., & Rauch, M. 1996, *ApJ*, 471, 582
- Monet, D., et al. 1996, *USNO-SA2.0*, U.S. Naval Observatory, Wash. DC
- Muller, G. P., et al. 1998, *SPIE*, 3355, 577
- Palunas, P., et al. 2000, *ApJ*, 541, 61
- Schlegel, D. J., Finkbeiner, D. P., and Davis, M. 1998, *ApJ*, 500, 525
- Turner, M. S. 2001, *PASP*, 113, 653
- Vanden Berk, D. E., et al. 1999, *ApJS*, 122, 355
- Vanden Berk, D. E., Stoughton, C., Crotts, A. P. S., Tytler, D., & Kirkman, D. 2000, *ApJ*, 119, 2571
- Williams, R. E., et al. 1996, *AJ*, 112, 1335
- Williams, R. E., et al. 2000, *AJ*, 120, 2735
- Williger, G. M., Hazard, C., Baldwin, J. A., & McMahon, R. G. 1996, *ApJS*, 104, 145
- Williger, G. M., Smette, A., Hazard, C., Baldwin, J. A., & McMahon, R. G. 2000, *ApJ*, 532, 77

TABLE 1  
JOURNAL OF OBSERVATIONS FOR THE J0053+1234 REGION

UT Date (1)	Filter (2)	$t_{\text{exp}}$ (3)	$N_{\text{exp}}$ (4)	Seeing (5)	Airmass (6)	Conditions (7)
30 Sep 1998	<i>U</i>	175	5	1.7	1.06 – 1.37	Mostly clear
	<i>B</i>	30	2	2.0	1.06 – 1.07	
	<i>B</i>	30	3	1.9	1.13 – 1.16	
	<i>R</i>	30	5	1.9	1.22 – 1.33	
	<i>I</i>	10	1	1.7	1.08	
01 Oct 1998	<i>U</i>	150	5	1.9	1.09 – 1.34	Mostly clear
	<i>I</i>	60	5	1.6	1.40 – 1.19	
02 Oct 1998	<i>U</i>	125	5	1.8	1.12 – 1.48	Some thin cirrus
	<i>B</i>	50	5	1.6	1.06 – 1.07	

NOTE.—Date of observation (1) and filter employed (2). The total exposure time in minutes (3), and the number of exposures for a dithered sequence of images (4). The estimated mean seeing FWHM in arcseconds (5), range of airmass values during each exposure sequence (6), and the conditions during the observations (7).

TABLE 2  
PHOTOMETRIC CALIBRATION PARAMETERS

Filter (1)	$\tilde{t}_{\text{exp}}$ (2)	$\tilde{X}$ (3)	Sky (4)	UT Date (5)	zp (6)	$\alpha$ (7)	$\beta$ (8)	RMS (9)
<i>U</i>	35	1.06	97	30 Sep 1998	$20.00 \pm 0.12$	$-0.51 \pm 0.09$	$+0.04 \pm 0.03$	0.051
<i>B</i>	10	1.06	462	30 Sep 1998	$21.70 \pm 0.07$	$-0.11 \pm 0.05$	$+0.12 \pm 0.01$	0.029
<i>R</i>	6	1.21	449	30 Sep 1998	$22.33 \pm 0.14$	$-0.33 \pm 0.10$	$+0.06 \pm 0.03$	0.036
<i>I</i>	12	1.19	1328	1 Oct 1998	$21.37 \pm 0.09$	$+0.01 \pm 0.06$	$+0.01 \pm 0.02$	0.030

NOTE.—The combined image parameters for each passband filter (1) are given: the effective image exposure time in minutes (2), the effective image airmass (3), and the scaled average of the background modes in ADUs (4). The transformation variables for photometric calibration are given for each filter: the UT date the photometric standards were observed (5), the magnitude zero point (6), the airmass coefficient (7), and the color term coefficient (8). The RMS in magnitudes (9) is given for the best-fit to the transformation equation.

TABLE 3  
UBRI SOURCE CATALOGS

Passband	99% Completeness Limit				90% Completeness Limit				
	$N_{\text{tot}}$	$m$	$N$	S/N	$m$	$N$	S/N	$m_{\text{TO}}$	Seeing
(1)	(2)	(3)	(4)	(5)	(6)	(7)	(8)	(9)	(10)
$U$	1946	20.7	1283	$\sim 25$	21.5	1754	$\sim 12$	21.0	1.7
$B$	2463	20.7	1575	$\sim 25$	21.7	2334	$\sim 11$	21.2	1.8
$R$	4505	19.5	2080	$\sim 33$	20.5	3678	$\sim 14$	20.2	1.9
$I$	7922	19.5	3493	$\sim 25$	20.5	6569	$\sim 11$	20.2	1.7

NOTE.—For each SExtractor generated catalog of passband (1), the total number of sources (2) following the removal of saturated and edge proximity objects (see text). The 99% point-source completeness limit magnitude (3), number of sources (4), and signal-to-noise limit (5). (6-8) give similar values for 90% point-source completeness. The magnitude at which source number counts turn over from steeply rising is in (9). The mean seeing FWHM in arcseconds for each combined image is in (10).

TABLE 4  
QUASAR SURVEY YIELD

Catalog	Number of Candidates	Number Observed	Number of Confirmed Quasars	Yield
(1)	(2)	(3)	(4)	(5)
UBRI – Region 1 <sup>a</sup>	58	57	43	75%
UBRI – Region 2 <sup>b</sup>	15	11	1	9%
UB <sup>c</sup>	32	30	16	53%
Combined	105	98	60	61%

<sup>a</sup>Objects with  $(U - B) \leq -0.2$  and  $(B - R) \leq 0.6$ ; Region 1 in Figure 2.

<sup>b</sup>Objects with  $(U - B) > -0.2$  and  $(B - R) \leq 0.4$ ; Region 2 in Figure 2.

<sup>c</sup>Objects with  $(U - B) \leq -0.1$ ; see Figure 4.

NOTE.—For each color selection criterion (1), the number of objects meeting that criterion (2), the number of objects actually observed (3), the number of quasars found (4), and the efficiency of finding quasars (5) for that criterion.

TABLE 5  
QUASARS IN THE J0053+1234 REGION

Name (1)	RA <sub>2000</sub> (2)	Dec <sub>2000</sub> (3)	$z$ (4)	$B$ (5)	$(U - B)$ (6)	$(B - R)$ (7)	$(R - I)$ (8)
Q005127+121931	00 51 26.94	+12 19 30.5	$1.027 \pm 0.007$	$20.65 \pm 0.04$	$-0.52 \pm 0.05$	$0.47 \pm 0.07$	$0.38 \pm 0.08$
Q005136+121303	00 51 36.29	+12 13 02.9	$1.735 \pm 0.003$	$19.09 \pm 0.01$	$-0.59 \pm 0.02$	$0.22 \pm 0.03$	$0.37 \pm 0.03$
Q005141+123050	00 51 40.90	+12 30 49.9	$0.686 \pm 0.011$	$19.97 \pm 0.03$	$-0.38 \pm 0.04$	$0.20 \pm 0.06$	$0.55 \pm 0.06$
Q005151+125239	00 51 50.57	+12 52 38.5	$2.076 \pm 0.001$	$20.66 \pm 0.06$	$-1.01 \pm 0.07$	$0.10 \pm 0.10$	$0.58 \pm 0.10$
Q005202+124501	00 52 02.50	+12 45 01.1	$2.119 \pm 0.001$	$21.11 \pm 0.08$	$-0.69 \pm 0.10$	...	...
Q005207+125404	00 52 06.68	+12 54 04.4	$1.200 \pm 0.010$	$20.75 \pm 0.06$	$-0.68 \pm 0.07$	$0.15 \pm 0.10$	$0.36 \pm 0.10$
Q005210+125114	00 52 10.10	+12 51 14.1	$2.127 \pm 0.001$	$21.14 \pm 0.08$	$-0.65 \pm 0.10$	...	...
Q005210+121023	00 52 10.36	+12 10 23.0	$1.656 \pm 0.006$	$21.04 \pm 0.07$	$-0.42 \pm 0.09$	...	...
Q005223+124754	00 52 22.57	+12 47 53.6	$1.447 \pm 0.007$	$21.03 \pm 0.08$	$-0.62 \pm 0.10$	...	...
Q005223+124627	00 52 23.28	+12 46 26.9	$2.386 \pm 0.001$	$20.85 \pm 0.06$	$-0.16 \pm 0.09$	...	...
Q005229+125717	00 52 29.49	+12 57 16.7	$1.435 \pm 0.008$	$19.88 \pm 0.03$	$-0.62 \pm 0.04$	$0.37 \pm 0.05$	$0.40 \pm 0.05$
Q005231+123137	00 52 30.61	+12 31 36.5	$1.311 \pm 0.006$	$18.87 \pm 0.01$	$-0.68 \pm 0.02$	$0.33 \pm 0.02$	$0.25 \pm 0.02$
Q005237+120538	00 52 36.65	+12 05 37.6	$0.801 \pm 0.009$	$20.74 \pm 0.07$	$-0.47 \pm 0.09$	$0.19 \pm 0.10$	$0.69 \pm 0.10$
Q005243+122048	00 52 42.68	+12 20 47.7	$1.255 \pm 0.009$	$20.84 \pm 0.06$	$-0.78 \pm 0.08$	$0.48 \pm 0.09$	$0.13 \pm 0.09$
Q005243+125613	00 52 43.23	+12 56 12.6	$0.809 \pm 0.009$	$17.45 \pm 0.01$	$-0.52 \pm 0.01$	$0.18 \pm 0.01$	$0.21 \pm 0.01$
Q005251+125819	00 52 50.51	+12 58 18.6	$0.954 \pm 0.008$	$18.65 \pm 0.01$	$-0.72 \pm 0.02$	$0.24 \pm 0.02$	$0.17 \pm 0.02$
Q005251+130112	00 52 50.83	+13 01 12.2	$1.904 \pm 0.004$	$19.40 \pm 0.02$	$-0.81 \pm 0.03$	$0.27 \pm 0.04$	$0.44 \pm 0.04$
Q005252+120705	00 52 52.01	+12 07 05.4	$0.638 \pm 0.009$	$21.05 \pm 0.08$	$-0.40 \pm 0.10$	$0.48 \pm 0.11$	$0.54 \pm 0.10$
Q005301+124538	00 53 00.95	+12 45 37.6	$0.872 \pm 0.007$	$21.27 \pm 0.08$	$-0.40 \pm 0.11$	...	...
Q005306+121551	00 53 05.59	+12 15 50.8	$2.318 \pm 0.003$	$21.50 \pm 0.09$	$-0.38 \pm 0.12$	...	...
Q005312+121816	00 53 12.42	+12 18 15.7	$1.662 \pm 0.007$	$20.56 \pm 0.05$	$-0.48 \pm 0.06$	$0.14 \pm 0.08$	$0.60 \pm 0.08$
Q005314+124518	00 53 13.99	+12 45 18.2	$1.631 \pm 0.007$	$20.68 \pm 0.05$	$-0.33 \pm 0.07$	$0.55 \pm 0.08$	$0.58 \pm 0.07$
Q005321+120923	00 53 20.61	+12 09 23.0	$0.805 \pm 0.008$	$21.35 \pm 0.09$	$-0.53 \pm 0.11$	...	...
Q005321+122740	00 53 21.41	+12 27 40.3	$0.546 \pm 0.006$	$19.12 \pm 0.01$	$-0.43 \pm 0.02$	$0.25 \pm 0.03$	$0.43 \pm 0.03$
Q005322+123101	00 53 22.26	+12 31 00.8	$1.115 \pm 0.010$	$21.61 \pm 0.10$	$-0.84 \pm 0.12$	...	...
Q005324+124233	00 53 24.24	+12 42 33.2	$2.146 \pm 0.001$	$20.07 \pm 0.03$	$-0.60 \pm 0.04$	$0.09 \pm 0.06$	$0.55 \pm 0.06$
Q005325+123344	00 53 24.59	+12 33 44.0	$0.679 \pm 0.009$	$19.89 \pm 0.03$	$-0.28 \pm 0.04$	$0.50 \pm 0.05$	$0.46 \pm 0.04$
Q005327+130224	00 53 27.00	+13 02 24.2	$1.182 \pm 0.010$	$19.83 \pm 0.03$	$-0.71 \pm 0.04$	$0.15 \pm 0.05$	$0.21 \pm 0.05$
Q005340+121859	00 53 40.09	+12 18 59.2	$0.771 \pm 0.010$	$19.32 \pm 0.02$	$-0.52 \pm 0.02$	$0.11 \pm 0.03$	$0.26 \pm 0.03$
Q005344+121847	00 53 43.51	+12 18 47.4	$0.622 \pm 0.010$	$19.42 \pm 0.02$	$-0.32 \pm 0.02$	$0.04 \pm 0.03$	$0.41 \pm 0.04$
Q005344+125844	00 53 43.54	+12 58 43.8	$0.655 \pm 0.007$	$20.14 \pm 0.04$	$-0.25 \pm 0.05$	$0.56 \pm 0.06$	$0.51 \pm 0.05$
Q005347+125455	00 53 46.95	+12 54 54.7	$0.592 \pm 0.011$	$19.60 \pm 0.03$	$-0.33 \pm 0.03$	$0.49 \pm 0.04$	$0.59 \pm 0.04$
Q005349+120826	00 53 49.19	+12 08 26.1	$1.332 \pm 0.006$	$20.93 \pm 0.05$	$-0.88 \pm 0.07$	$0.36 \pm 0.09$	$0.24 \pm 0.10$
Q005355+121232	00 53 54.71	+12 12 31.5	$2.089 \pm 0.001$	$21.64 \pm 0.10$	$-0.80 \pm 0.13$	...	...
Q005358+123038	00 53 57.57	+12 30 37.9	$0.804 \pm 0.009$	$21.31 \pm 0.08$	$-0.58 \pm 0.10$	...	...
Q005358+124744	00 53 57.69	+12 47 44.4	$2.103 \pm 0.001$	$20.73 \pm 0.07$	$-0.50 \pm 0.09$	...	...
Q005405+123031	00 54 04.96	+12 30 31.3	$1.574 \pm 0.005$	$20.07 \pm 0.03$	$-0.48 \pm 0.04$	$0.38 \pm 0.04$	$0.35 \pm 0.04$
Q005405+130403	00 54 05.14	+13 04 02.6	$1.824 \pm 0.006$	$19.46 \pm 0.02$	$-0.74 \pm 0.03$	$-0.01 \pm 0.04$	$0.43 \pm 0.04$
Q005408+122909	00 54 08.19	+12 29 09.3	$1.162 \pm 0.010$	$20.65 \pm 0.04$	$-0.85 \pm 0.06$	$0.59 \pm 0.07$	$0.08 \pm 0.07$
Q005410+125613	00 54 09.58	+12 56 13.1	$1.368 \pm 0.009$	$20.47 \pm 0.05$	$-0.62 \pm 0.06$	$-0.06 \pm 0.09$	$0.31 \pm 0.10$
Q005414+123349	00 54 14.05	+12 33 48.9	$2.098 \pm 0.001$	$19.36 \pm 0.02$	$-0.59 \pm 0.02$	$0.27 \pm 0.03$	$0.31 \pm 0.03$
Q005425+124215	00 54 24.81	+12 42 15.5	$1.132 \pm 0.010$	$19.71 \pm 0.02$	$-0.59 \pm 0.03$	$0.31 \pm 0.04$	$0.22 \pm 0.04$
Q005428+122003	00 54 27.74	+12 20 02.6	$1.725 \pm 0.005$	$21.21 \pm 0.07$	$-0.52 \pm 0.10$	...	...
Q005428+124427	00 54 27.79	+12 44 27.1	$2.200 \pm 0.001$	$20.81 \pm 0.06$	$-0.48 \pm 0.08$	...	...
Q005433+121853	00 54 33.15	+12 18 53.1	$1.699 \pm 0.005$	$21.00 \pm 0.07$	$-0.32 \pm 0.09$	$0.20 \pm 0.12$	$0.55 \pm 0.11$
Q005444+124732	00 54 44.47	+12 47 31.8	$1.286 \pm 0.007$	$20.91 \pm 0.07$	$-0.88 \pm 0.08$	$0.32 \pm 0.11$	$0.43 \pm 0.11$
Q005445+125313	00 54 44.79	+12 53 13.3	$2.124 \pm 0.001$	$20.23 \pm 0.04$	$-0.78 \pm 0.05$	$0.20 \pm 0.07$	$0.57 \pm 0.06$
Q005445+125402	00 54 45.15	+12 54 02.0	$0.868 \pm 0.011$	$19.74 \pm 0.03$	$-0.55 \pm 0.04$	$0.24 \pm 0.05$	$0.21 \pm 0.05$
Q005448+121848	00 54 47.75	+12 18 47.7	$0.924 \pm 0.007$	$21.00 \pm 0.07$	$-0.48 \pm 0.09$	$0.48 \pm 0.11$	$0.71 \pm 0.10$
Q005451+124332	00 54 50.86	+12 43 32.1	$1.281 \pm 0.009$	$21.13 \pm 0.08$	$-0.58 \pm 0.09$	$0.51 \pm 0.12$	$0.23 \pm 0.11$

TABLE 5—*Continued*

Name (1)	RA <sub>2000</sub> (2)	Dec <sub>2000</sub> (3)	$z$ (4)	$B$ (5)	$(U - B)$ (6)	$(B - R)$ (7)	$(R - I)$ (8)
Q005454+130231	00 54 54.18	+13 02 30.6	$0.496 \pm 0.012$	$21.40 \pm 0.09$	$-0.62 \pm 0.12$	...	...
Q005457+121857	00 54 57.30	+12 18 57.0	$1.804 \pm 0.005$	$20.86 \pm 0.06$	$-0.59 \pm 0.07$	$0.32 \pm 0.10$	$0.49 \pm 0.10$
Q005458+123706	00 54 58.23	+12 37 05.5	$1.868 \pm 0.005$	$21.64 \pm 0.10$	$-0.72 \pm 0.12$	...	...
Q005459+130230	00 54 58.93	+13 02 29.6	$1.429 \pm 0.007$	$20.97 \pm 0.08$	$-0.71 \pm 0.09$	$0.29 \pm 0.11$	$0.25 \pm 0.12$
Q005501+123338	00 55 01.12	+12 33 38.1	$1.293 \pm 0.006$	$20.31 \pm 0.04$	$-0.63 \pm 0.05$	$0.50 \pm 0.06$	$0.04 \pm 0.06$
Q005501+125932	00 55 01.48	+12 59 31.8	$1.516 \pm 0.006$	$20.18 \pm 0.04$	$-0.73 \pm 0.05$	$0.44 \pm 0.06$	$0.22 \pm 0.06$
Q005504+121402	00 55 04.29	+12 14 02.1	$1.145 \pm 0.008$	$20.09 \pm 0.03$	$-0.71 \pm 0.04$	$0.36 \pm 0.04$	$0.10 \pm 0.05$
Q005510+124910	00 55 09.89	+12 49 09.8	$2.292 \pm 0.002$	$20.07 \pm 0.03$	$-0.18 \pm 0.05$	$0.28 \pm 0.05$	$0.34 \pm 0.05$
Q005514+122400	00 55 13.82	+12 23 59.7	$1.137 \pm 0.010$	$20.40 \pm 0.05$	$-0.64 \pm 0.06$	$0.14 \pm 0.07$	$0.26 \pm 0.08$
Q005520+123317	00 55 19.87	+12 33 17.4	$1.857 \pm 0.005$	$19.74 \pm 0.03$	$-0.63 \pm 0.04$	$0.17 \pm 0.05$	$0.39 \pm 0.05$

NOTE.—For each new confirmed quasar (1), the J2000 coordinates (2) and (3), the measured redshift and error (4), the  $B$  band brightness in magnitudes (5), and the measured  $U - B$  (6),  $B - R$  (7), and  $R - I$  (8) colors in magnitudes.

TABLE 6  
EMISSION LINE GALAXIES IN THE J0053+1234 REGION

Name (1)	RA <sub>2000</sub> (2)	Dec <sub>2000</sub> (3)	$z$ (4)	$B$ (5)	$(U - B)$ (6)	$(B - R)$ (7)	$(R - I)$ (8)
Q005212+120851	00 52 11.98	+12 08 50.8	$0.1142 \pm 0.0005$	$21.00 \pm 0.08$	$-0.07 \pm 0.11$	$0.18 \pm 0.13$	$0.60 \pm 0.12$
Q005247+130321	00 52 47.20	+13 03 20.9	$0.1906 \pm 0.0004$	$20.95 \pm 0.07$	$-0.81 \pm 0.09$	$0.39 \pm 0.11$	$0.63 \pm 0.11$
Q005249+122433	00 52 48.71	+12 24 33.1	$0.1914 \pm 0.0005$	$21.39 \pm 0.08$	$-0.28 \pm 0.12$	...	...
Q005255+125842	00 52 54.75	+12 58 42.3	$0.0788 \pm 0.0005$	$20.28 \pm 0.06$	$-0.25 \pm 0.08$	$0.47 \pm 0.08$	$0.42 \pm 0.08$
Q005323+121946	00 53 23.22	+12 19 45.9	$0.1031 \pm 0.0005$	$21.69 \pm 0.11$	$-0.79 \pm 0.14$	...	...
Q005334+123353	00 53 33.59	+12 33 52.9	$0.0576 \pm 0.0004$	$20.77 \pm 0.06$	$-0.33 \pm 0.10$	...	...
Q005336+125611	00 53 36.25	+12 56 10.6	$0.0305 \pm 0.0006$	$20.46 \pm 0.06$	$-0.11 \pm 0.08$	$0.48 \pm 0.09$	$0.43 \pm 0.09$
Q005339+125158	00 53 38.87	+12 51 57.9	$0.1132 \pm 0.0005$	$20.85 \pm 0.07$	$-0.25 \pm 0.10$	$0.32 \pm 0.11$	$0.53 \pm 0.10$
Q005347+124450	00 53 46.96	+12 44 49.9	$0.0796 \pm 0.0004$	$19.88 \pm 0.04$	$-0.08 \pm 0.06$	$0.53 \pm 0.06$	$0.39 \pm 0.06$
Q005406+125338	00 54 06.44	+12 53 38.0	$0.3148 \pm 0.0103$	$20.70 \pm 0.07$	$-0.33 \pm 0.10$	...	...
Q005420+123159	00 54 20.33	+12 31 59.2	$0.1914 \pm 0.0005$	$21.40 \pm 0.09$	$-0.26 \pm 0.12$	$0.59 \pm 0.13$	$0.52 \pm 0.11$
Q005436+122318	00 54 36.47	+12 23 17.8	$0.0382 \pm 0.0018$	...	...	...	...
Q005500+122941	00 55 00.25	+12 29 40.7	$0.0719 \pm 0.0006$	$20.64 \pm 0.05$	$-0.06 \pm 0.08$	$0.38 \pm 0.08$	$0.60 \pm 0.08$
Q005520+123421	00 55 19.52	+12 34 20.9	$0.1783 \pm 0.0004$	$20.81 \pm 0.07$	$-0.16 \pm 0.10$	$0.53 \pm 0.11$	$0.48 \pm 0.09$

NOTE.—For each new emission line galaxy (1), the J2000 coordinates (2) and (3), the measured redshift and error (4), the  $B$  band brightness in magnitudes (5), and the measured  $U - B$  (6),  $B - R$  (7), and  $R - I$  (8) colors in magnitudes.



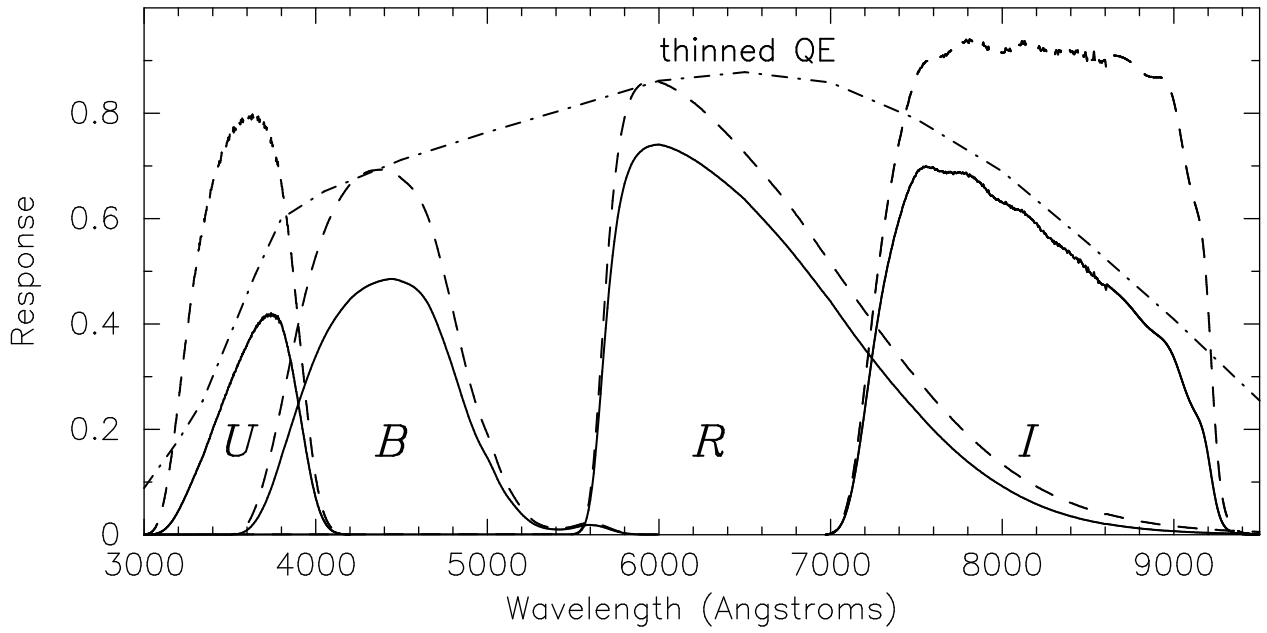


Fig. 1.— Average KPNO Mosaic response in the *UBRI* passbands (solid lines). The dash-dotted line represents the average quantum efficiency (QE) of the eight Mosaic Loral CCD's. The transmission of each filter is given by the dashed lines. The total response is the combination of the filter transmission and QE. The *U*-band response of the system used for our observations drops off rapidly blueward of  $\sim 3750$  Å.

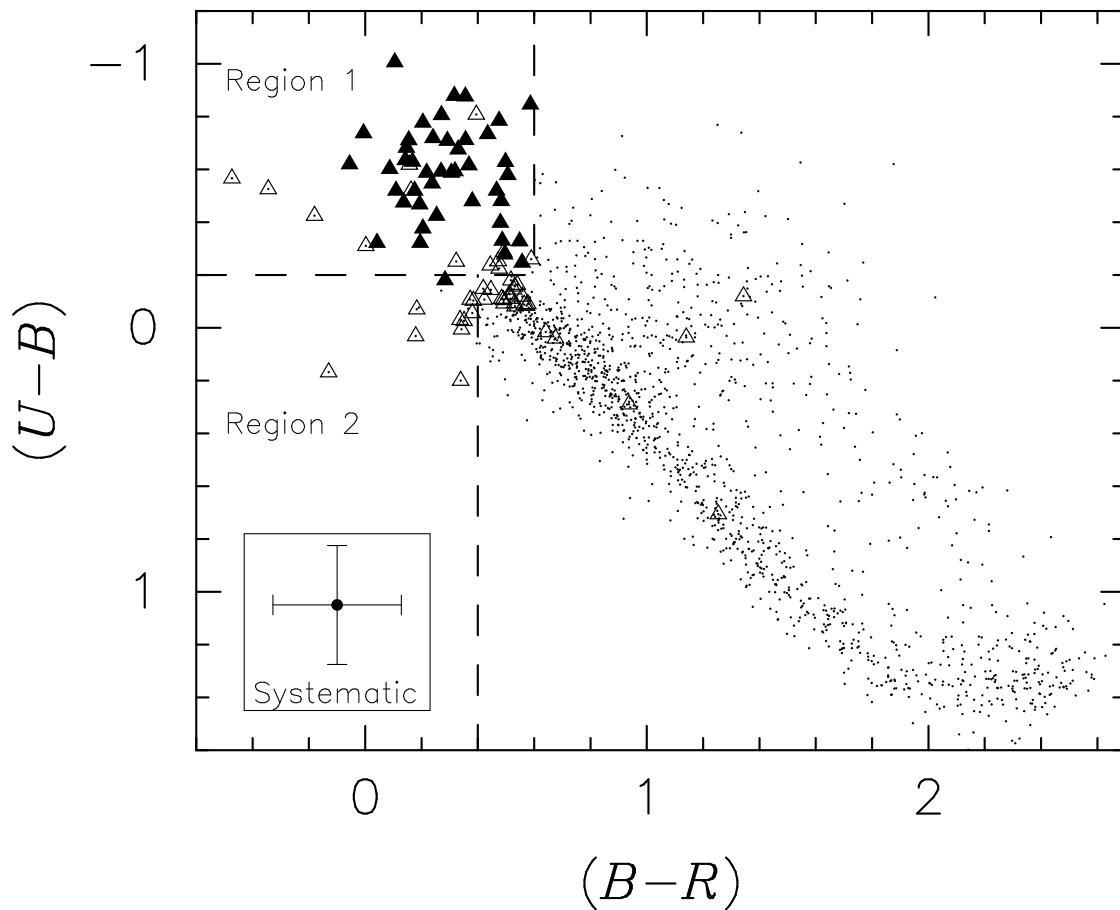


Fig. 2.— Multi-color photometry of the J0053+1234 field.  $(U - B)$  versus  $(B - R)$  color-color plot for the 1552 sources with  $UBRI$  photometry. The photometry presented here has been corrected for airmass and color terms, as well as Galactic extinction using the Schlegel, Finkbeiner & Davis (1998) reddening maps. The average systematic color errors, which dominate over random photometric errors, are given in the lower left box. There are 44 spectroscopically confirmed quasars (solid triangles) and 48 confirmed non-quasi-stellar objects (open triangles). The boundary (dashed line) represents the estimated end of the stellar locus; therefore, sources bluer than this are likely quasars (see text for details).

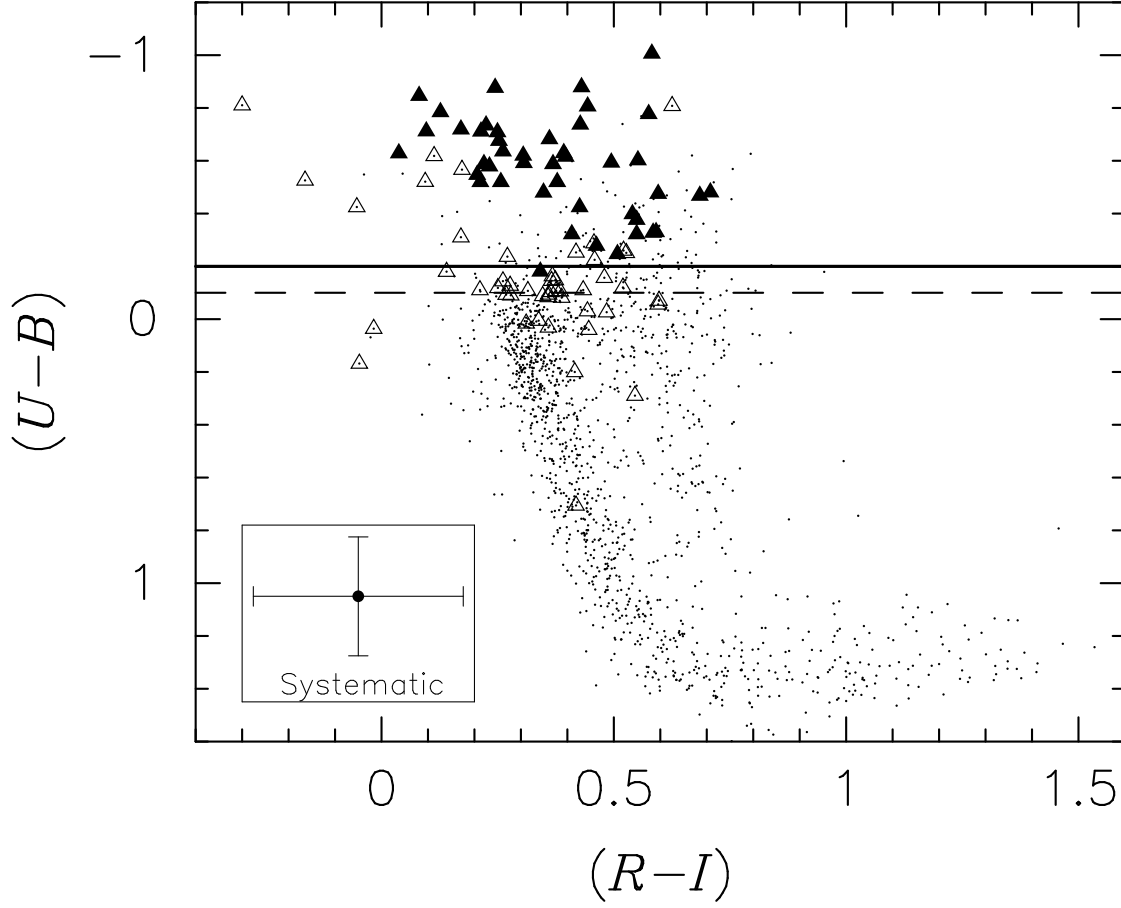


Fig. 3.— Multi-color photometry of the J0053+1234 field.  $(U - B)$  versus  $(R - I)$  color-color plot for the 1552 sources with  $UBRI$  photometry. The photometry presented here has been corrected for airmass and color terms, as well as Galactic extinction using the Schlegel, Finkbeiner & Davis (1998) reddening maps. The mean systematic color errors, which dominate over random photometric errors, are given in box at the lower left. A cut of  $B < 21.3$  is applied to keep random photometric errors low enough that the stellar locus is well-defined. As in Figure 2, the 44 spectroscopically confirmed quasars (solid triangles) and 48 confirmed non-quasi-stellar objects (open triangles) are shown. We show the  $(U - B) \leq -0.2$  (solid line) and  $(U - B) \leq -0.1$  (dashed line) boundaries.

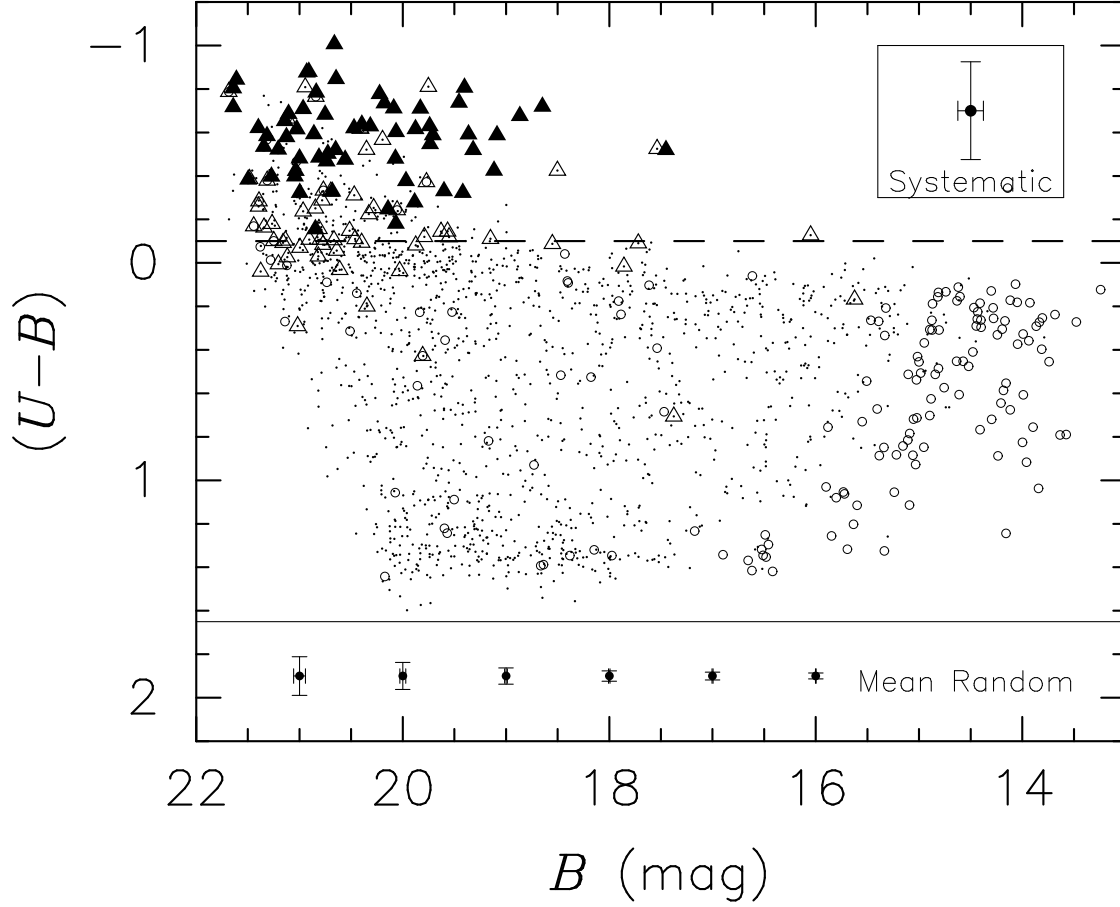
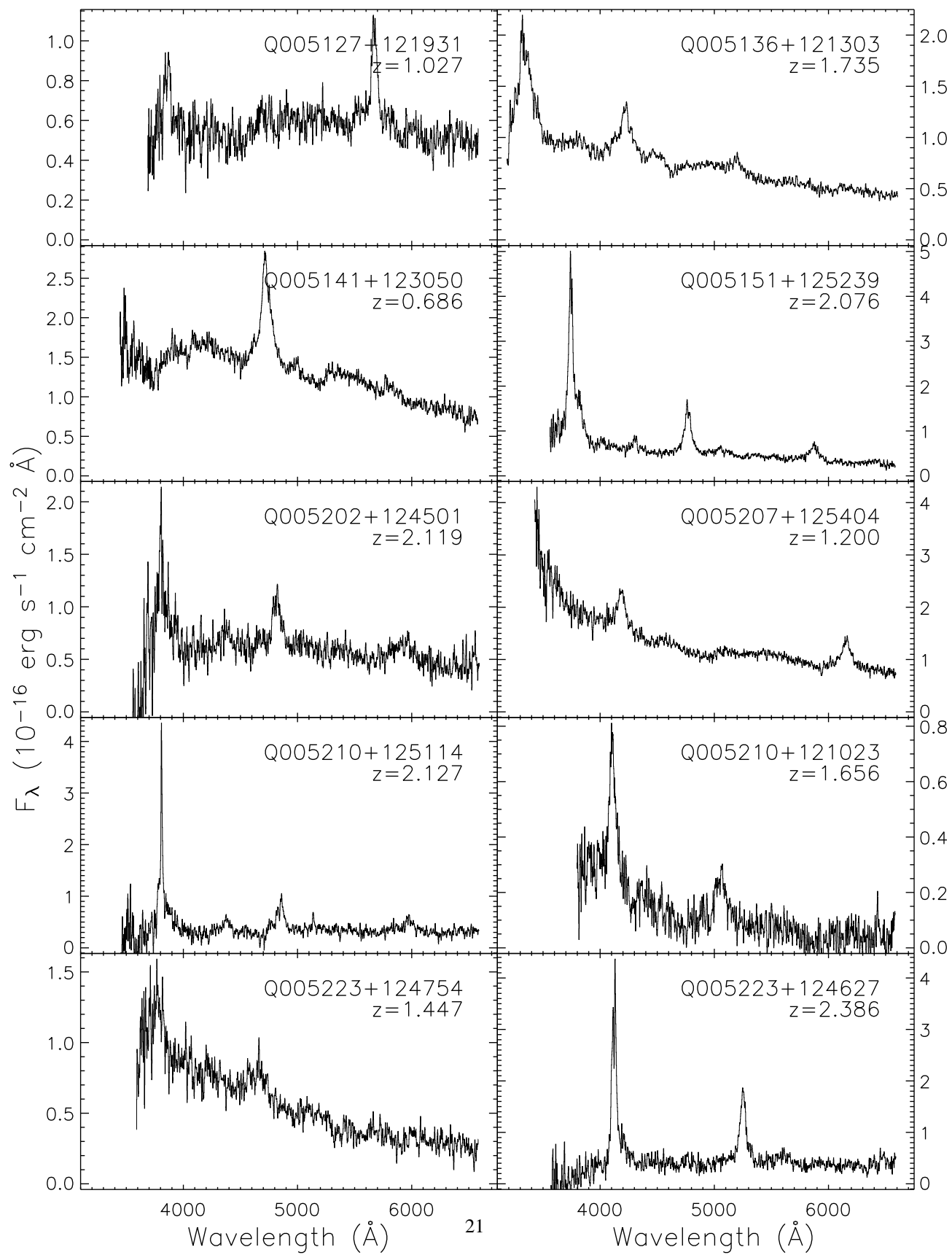
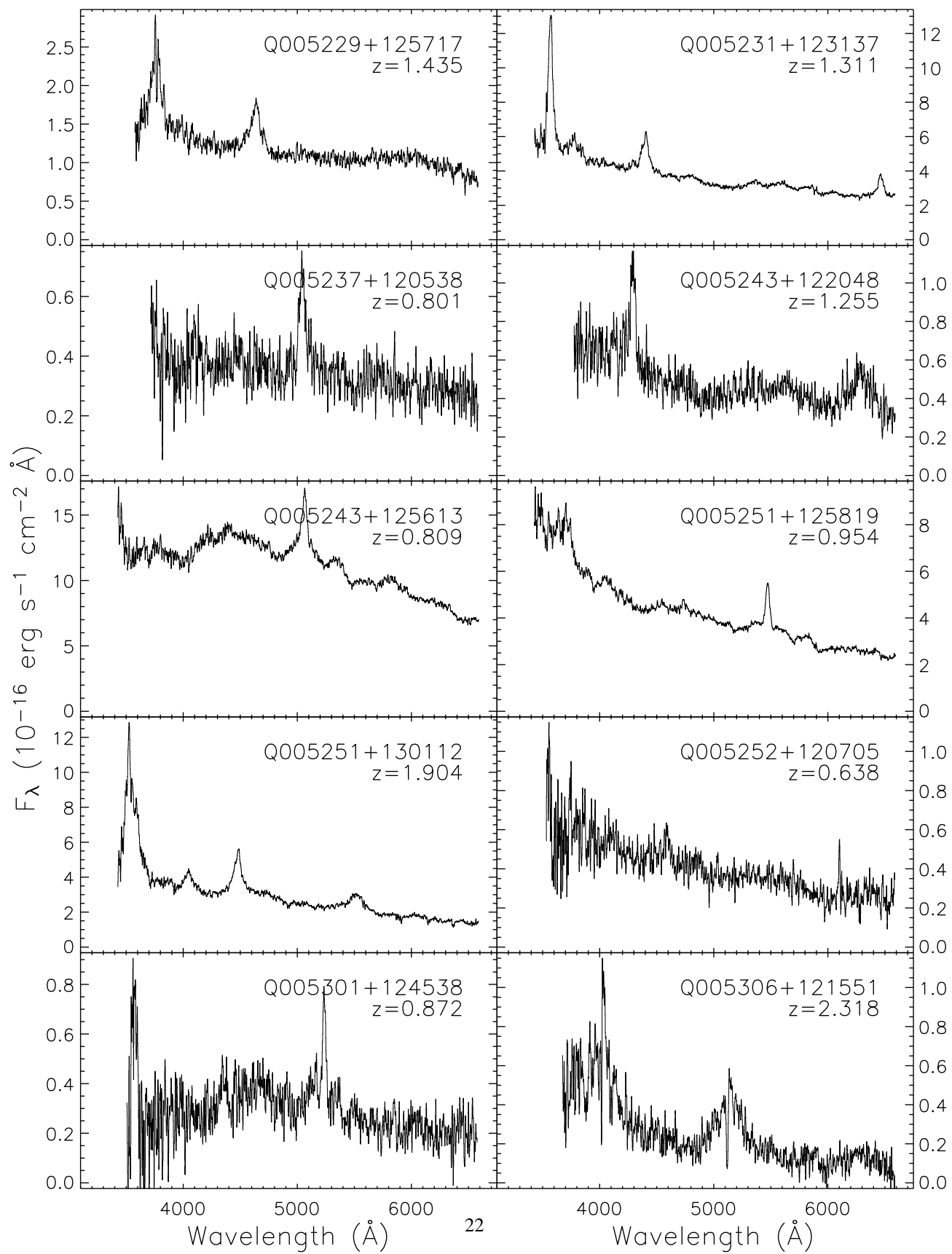
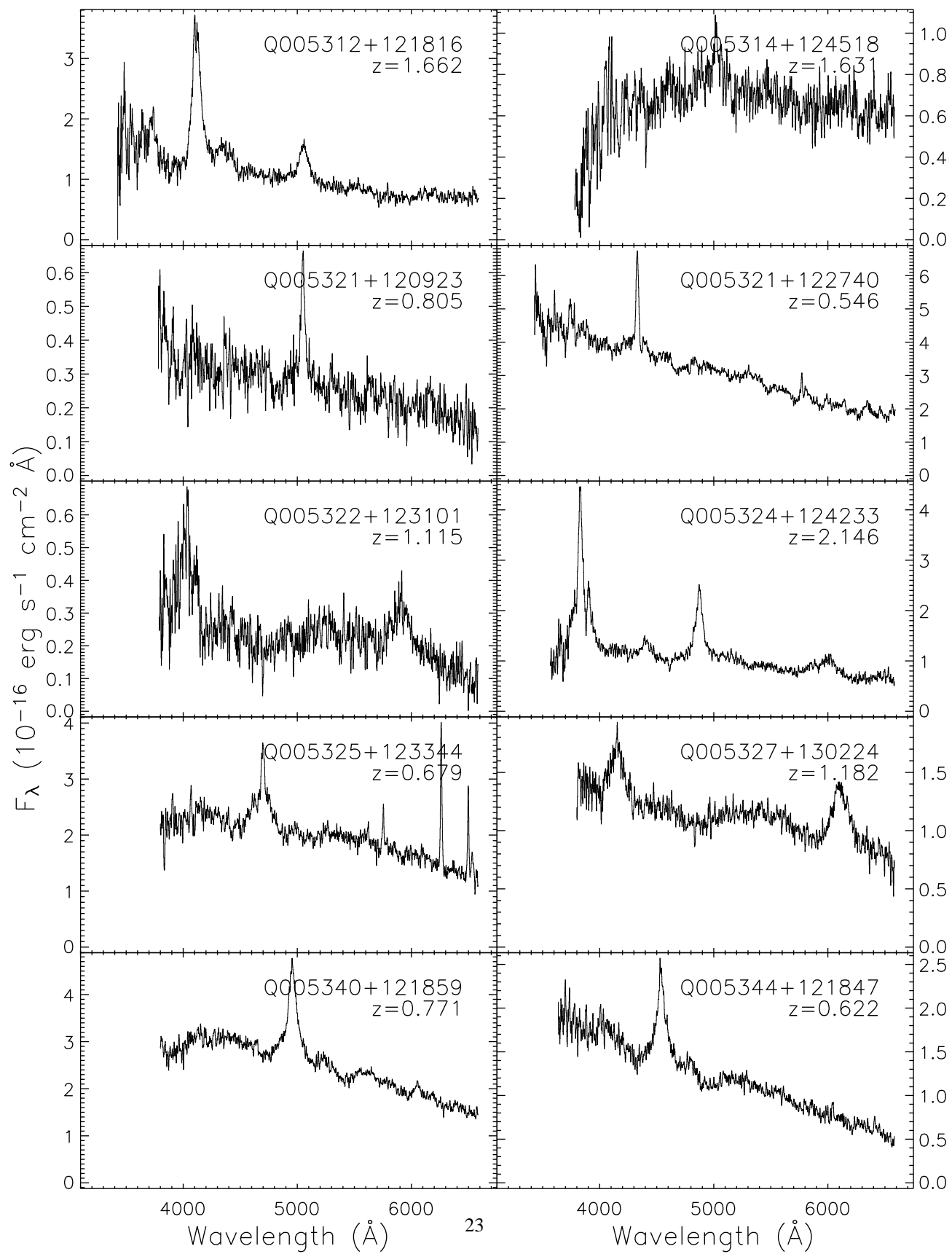
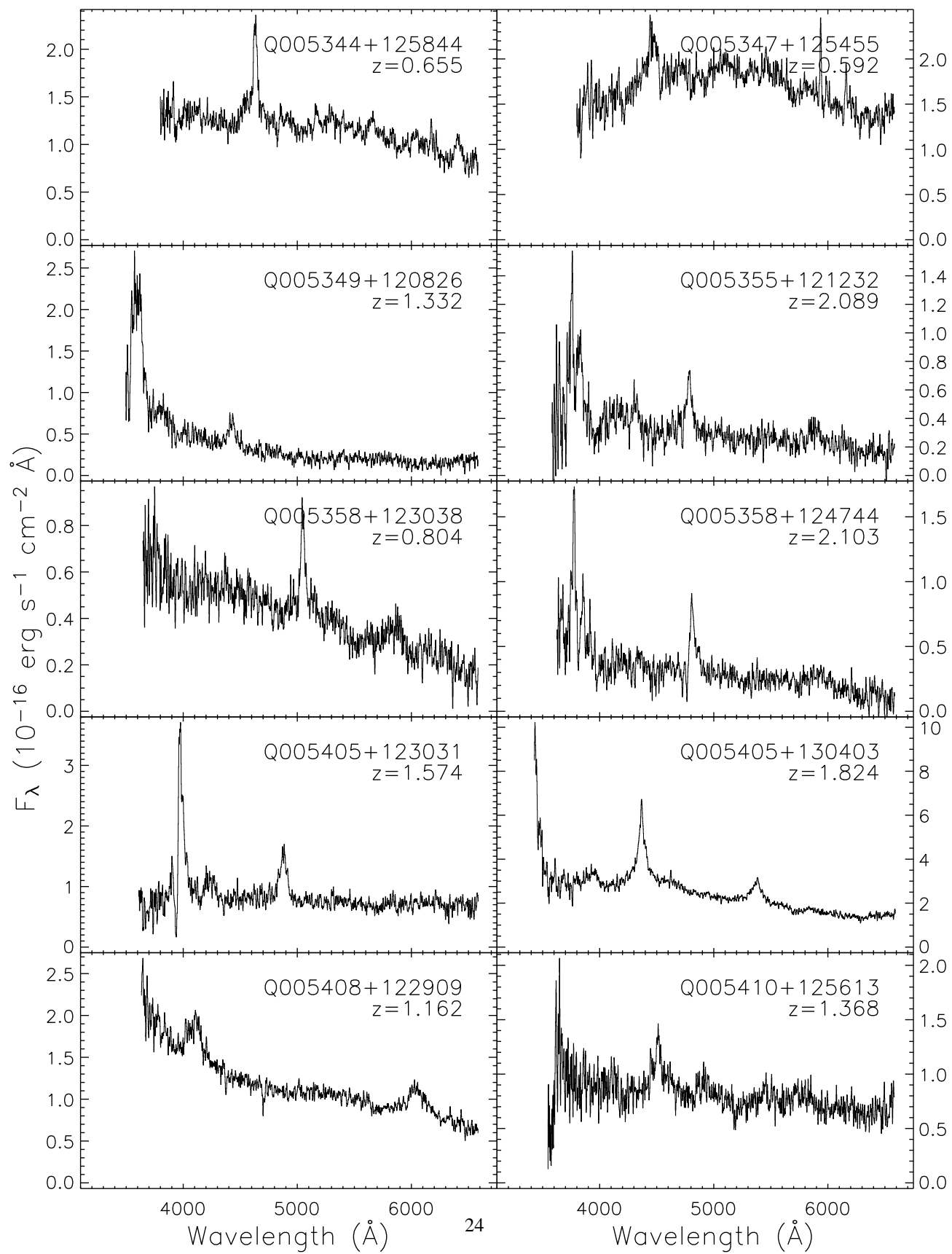


Fig. 4.—  $U, B$  color-magnitude diagram of 1730 sources from the J0053+1234 field, showing 178 sources with only  $U, B$  detections (small open circles), and 1552 with  $UBRI$  photometry (small dots). Sources with spectroscopic observations are shown as triangles, they comprise 60 confirmed quasars (solid triangles) and 62 nonquasi-stellar objects (open triangles). One quarter (30/122) of the spectroscopic targets are  $UB$ -only sources, and 16 of these are confirmed quasars. The dashed line shows the blue ( $U - B$ ) color cut for objects with  $R$  and  $I$  non-detections. The photometry presented here has been corrected for airmass and color terms, as well as Galactic extinction using the Schlegel, Finkbeiner & Davis (1998) reddening maps. We show the mean systematic error in photometry in the upper right-hand box. The random photometric errors as a function of  $B$  magnitude are given at the bottom.

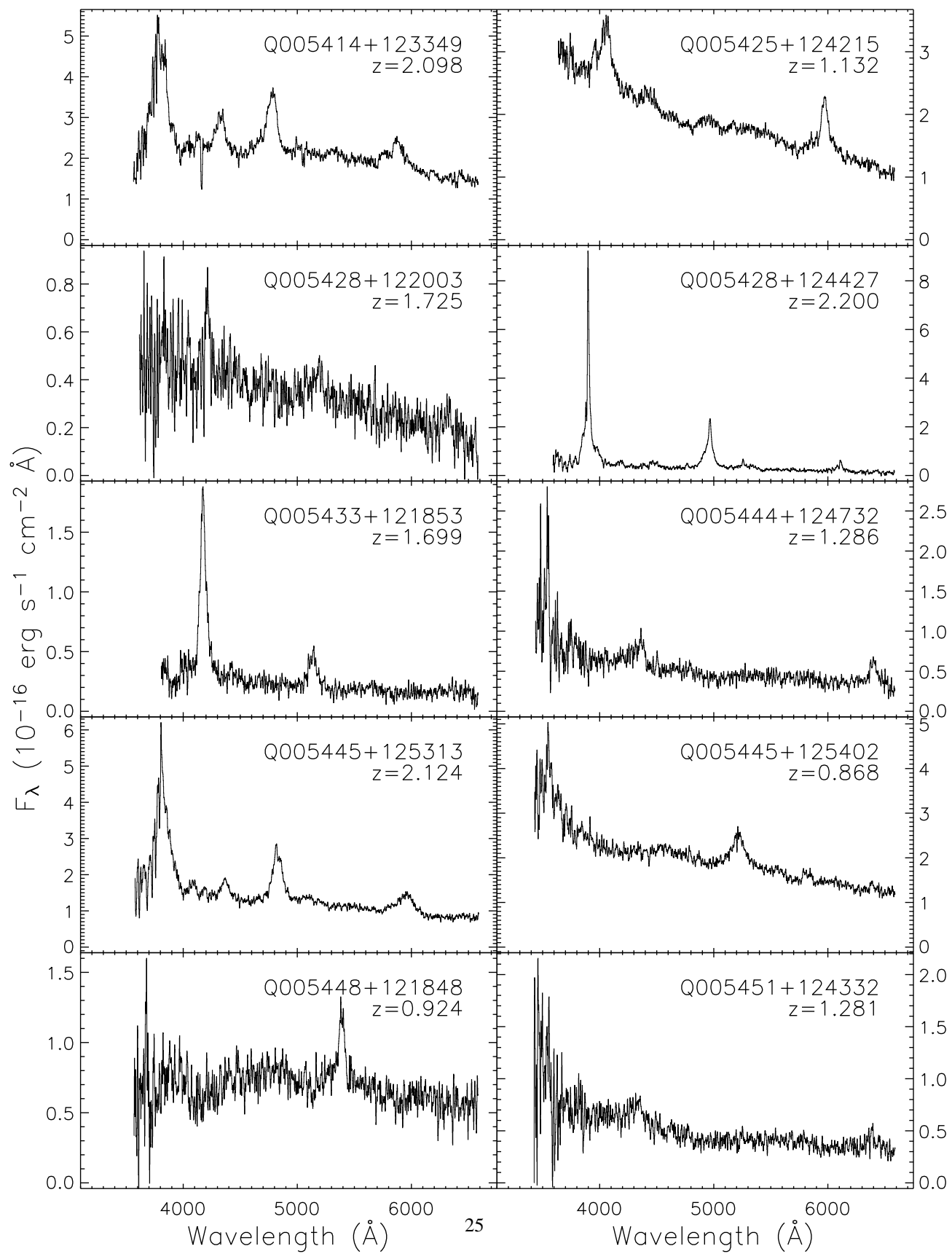












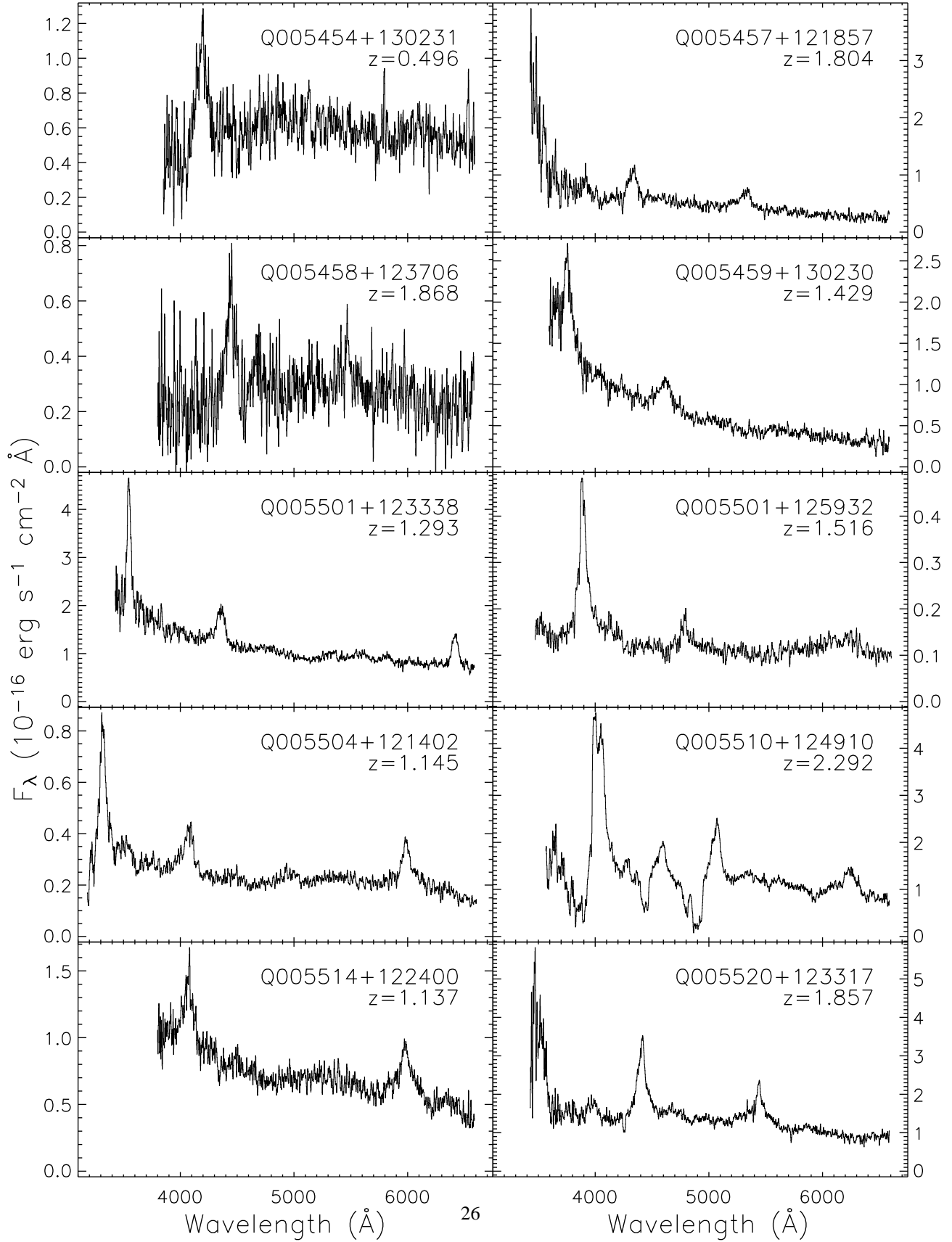


Fig. 5.— Spectra of 60 newly confirmed quasars plotted in R.A. order from left to right and down the page. Although the spectra have been flux calibrated, the spectrophotometry is only accurate to about 30%.

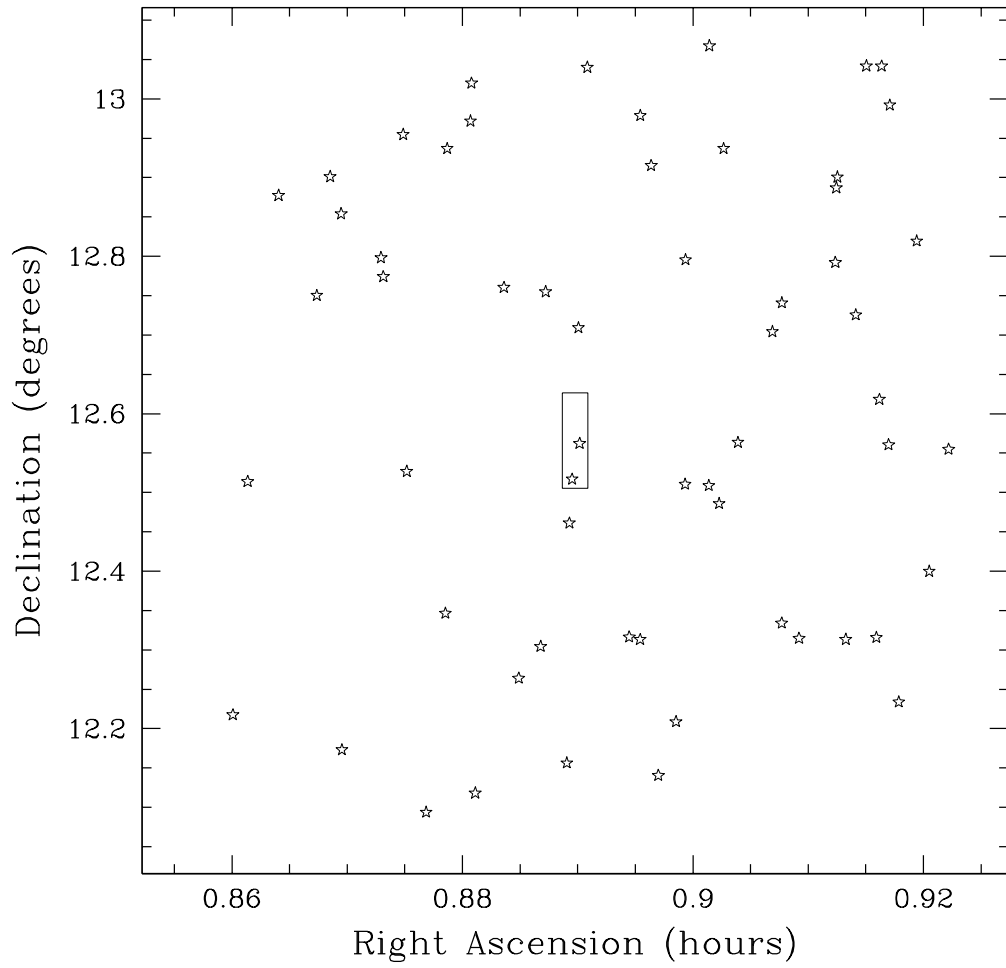
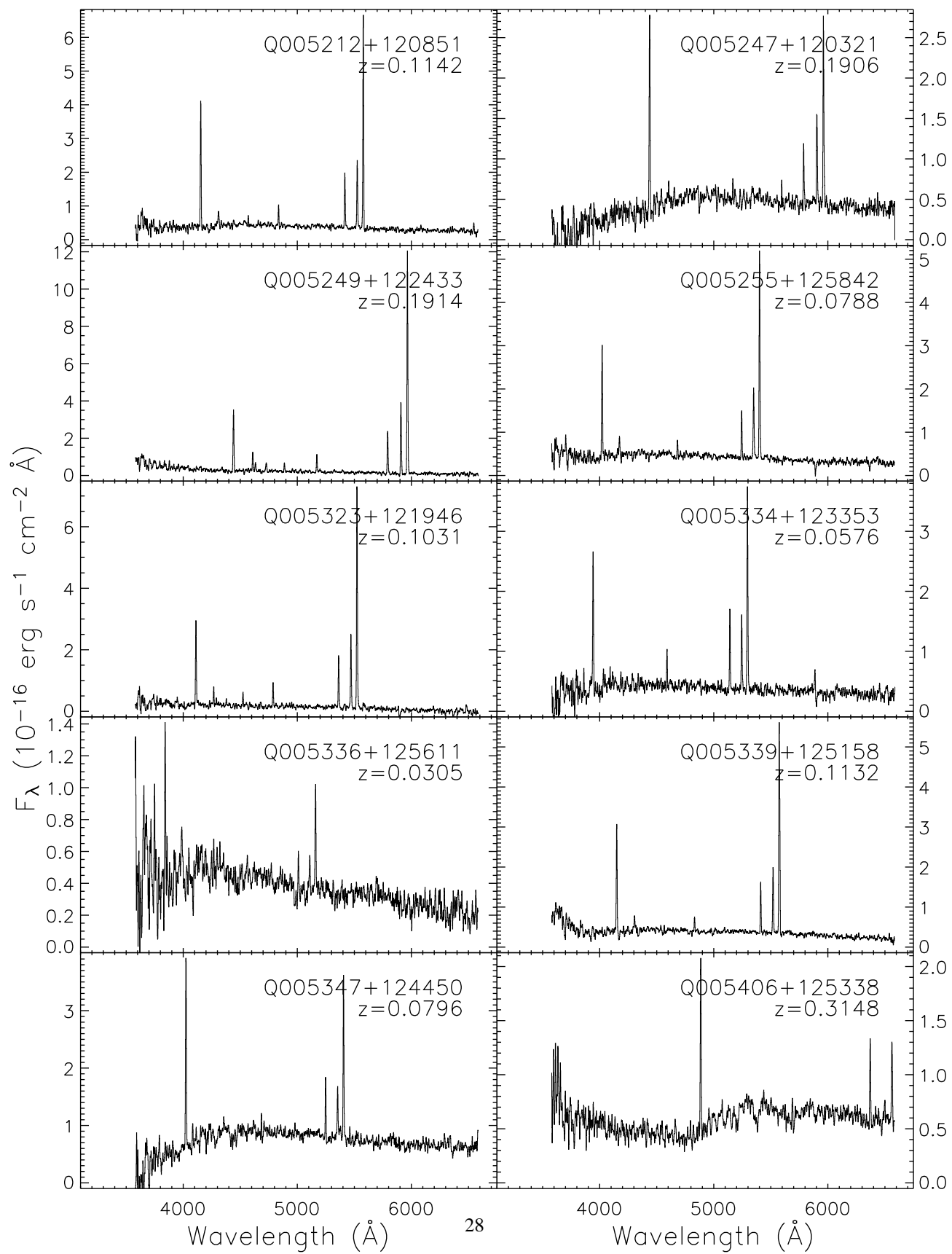


Fig. 6.— A sky map of the 60 quasars found in this survey. The rectangle in the center of the plot denotes the boundary of the  $2' \times 7/33$  Cohen et al. (1999a) galaxy survey.



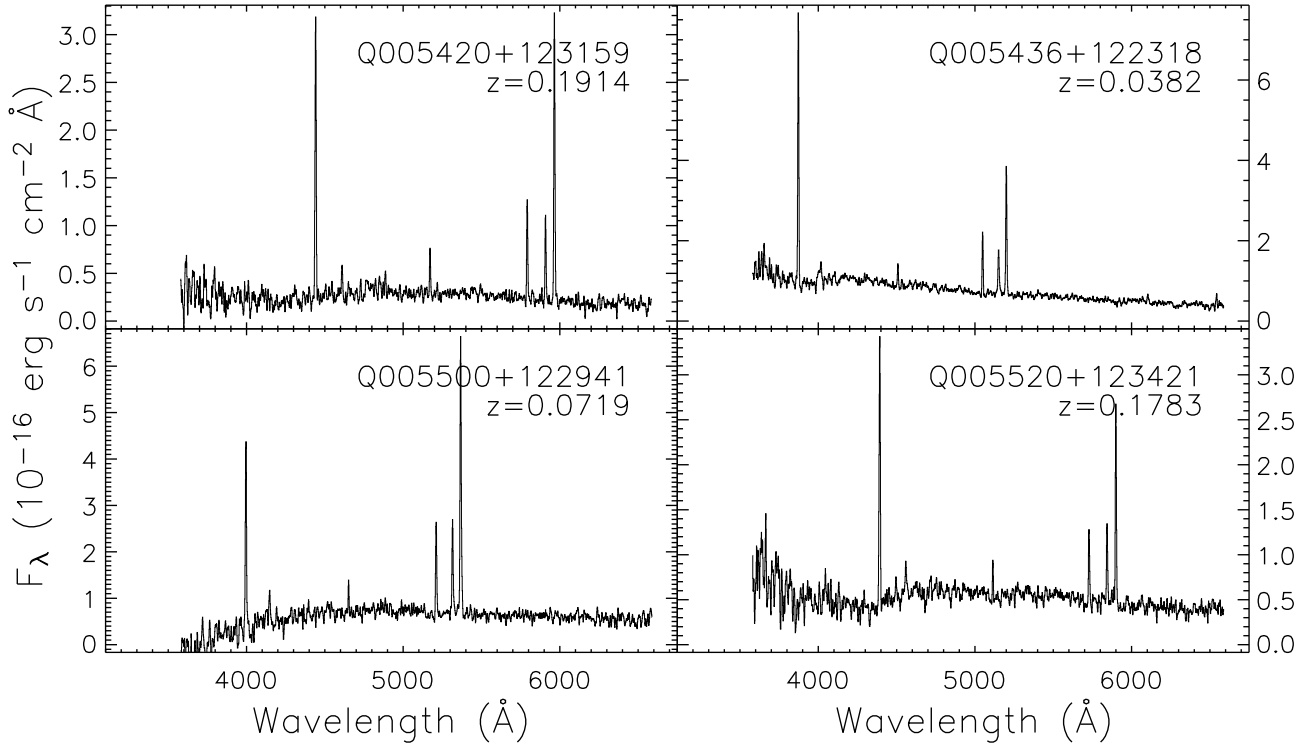


Fig. 7.— Spectra of 14 new emission line galaxies plotted in R.A. order from left to right and down the page. Although the spectra have been flux calibrated, the spectrophotometry is only accurate to about 30%.